



doi:10.1016/j.gca.2003.11.021

## Natural speciation of Zn at the micrometer scale in a clayey soil using X-ray fluorescence, absorption, and diffraction

ALAIN MANCEAU,<sup>1,\*</sup> MATTHEW A. MARCUS,<sup>2</sup> NOBUMICHI TAMURA,<sup>2</sup> OLIVIER PROUX,<sup>1,3</sup> NICOLAS GEOFFROY,<sup>1</sup> and BRUNO LANSON<sup>1</sup><sup>1</sup>Environmental Geochemistry Group, Maison des Géosciences, Univ. J. Fourier, BP 53, 38041 Grenoble Cedex 9, France<sup>2</sup>Advanced Light Source, Lawrence Berkeley National Laboratory, One Cyclotron Road, Berkeley, CA 94720, USA<sup>3</sup>FAME-CRG, European Synchrotron Radiation Facility, BP 220, 38043 Grenoble Cedex, France

(Received July 24, 2003; accepted in revised form November 21, 2003)

**Abstract**—Combined use of synchrotron-based X-ray fluorescence (SXRF), diffraction (XRD), and absorption (EXAFS) with an X-ray spot size as small as five micrometers allows us to examine noninvasively heterogeneous soils and sediments. Specifically, the speciation of trace metals at low bulk concentrations and the nature of host minerals can be probed with a level of detail unattainable by other techniques. The potential of this novel analytical approach is demonstrated by determining the Zn species in the solid phases of a pristine horizon of a clayey acidic soil (pH 4.5–5.0) having a Zn concentration of 128 mg/kg. The sample presents a differentiated fabric under the optical microscope with traces of localized manganiferous, ferriferous and argillaceous accumulations. The high chemical and textural heterogeneity of this soil offers an opportunity to identify new Zn species and to confirm the existence of others proposed from published least-squares fits of bulk averaged EXAFS spectra. As many as five to six Zn species were observed: sphalerite (ZnS), zincochromite (ZnCr<sub>2</sub>O<sub>4</sub>), Zn-containing phyllosilicate and lithiophorite, and Zn-sorbed ferrihydrite or Zn-phosphate, the results being less definitive for these two last species. Bulk EXAFS spectroscopy applied to the powdered soil indicated that Zn is predominantly associated with phyllosilicates, all other species amounting to < ~10 to 20% of total zinc. The role of lithiophorite in the sequestration of zinc in soils had been inferred previously, but the firm identification of lithiophorite in this study serves as an excellent demonstration of the capabilities of combined micro-SXRF/XRD/EXAFS measurements. The micro-EXAFS spectrum collected in an area containing only phyllosilicates could not be simulated assuming a single Zn structural environment. Two distinct octahedrally-coordinated crystallographic sites (i.e., two EXAFS components) were considered: one site located within the phyllosilicate structure (isomorphic cationic substitution in the octahedral sheet) and another in the interlayer region in the form of a Zn-sorbed hydroxy-Al interlayered species. This second subspecies is less certain and further investigation of the individual EXAFS spectrum of this component is needed to precise its exact nature and the uptake mechanism of zinc in it. Copyright © 2004 Elsevier Ltd

### 1. INTRODUCTION

Zinc contamination of surficial environments is a general concern of industrialized countries (Adriano, 1986; Robson, 1993). Since metal toxicity primarily depends on metal speciation, determining the forms of zinc in soils and sediments has gained attention recently, especially with regard to mitigating zinc's impact on ecosystems. This collective effort has already resulted in identification of a large number of primary (generally anhydrous inherited minerals) and secondary (generally hydroxylated minerals resulting from the weathering of primary minerals) Zn species. Primary minerals include sphalerite (ZnS), franklinite (ZnFe<sub>2</sub>O<sub>4</sub>), Zn-containing magnetite ([Fe,Zn]Fe<sub>2</sub>O<sub>4</sub>), willemite (Zn<sub>2</sub>SiO<sub>4</sub>), hemimorphite (Zn<sub>4</sub>Si<sub>2</sub>O<sub>7</sub>[OH]<sub>2</sub> · H<sub>2</sub>O), and zincite (ZnO), with sphalerite being by far the most abundant since it is encountered both in contaminated and uncontaminated soils and sediments (Luther et al., 1980; Parkman et al., 1996; O'Day et al., 1998, 2000; Manceau et al., 2000a; Gaillard et al., 2001; Carroll et al., 2002; Isaure et al., 2002, 2003; Roberts et al., 2002; Kirpichtchikova et al., 2003). Under oxidizing conditions, sphalerite is unstable and often represents the main source of dissolved Zn<sup>2+</sup> (Luther et al., 1996). With the noticeable exception of strongly acidic soils, in which aqueous Zn<sup>2+</sup> partly forms

weakly bound complexes, zinc is either known or thought to be precipitated as or taken up by a variety of secondary minerals including phosphate, phyllosilicate, ferrihydrite, goethite, birmessite, lithiophorite, hydrozincite, and hydrotalcite (Manceau et al., 2000a, 2000b, 2003; Hansel et al., 2001; Roberts et al., 2002; Scheinost et al., 2002; Isaure et al., 2003; Juillot et al., 2003; Kirpichtchikova et al., 2003). In phyllosilicates, zinc may be incorporated in, or sorbed on, the octahedral sheet or a hydroxy-Al sheet in the interlayer region (Scheinost et al., 2002).

In all soils and sediments studied so far, zinc was always present in several forms, and previous investigators outlined the overwhelming difficulty of characterizing in full the nature and proportions of all the existing forms. The high variability of Zn speciation, especially in the inorganic fraction of soils, contrasts for example with the strong association of As with Fe (oxyhydr)oxides and Pb with Mn oxides at the earth's surface. The multiplicity of Zn forms probably has no equivalent among other metal and metalloid contaminants. The main reason for the specific crystal chemical behavior of zinc is twofold. First, zinc may enter soils through many different natural and anthropogenic routes and, hence, various forms, which widens the total spectrum of Zn species relative to background species originally present in soil. For example, anthropogenic zinc may result from a number of agricultural practices (e.g., fertilization, pesticide sprays, irrigation with sewage sludges, soil

\* Author to whom correspondence should be addressed (alain.manceau@ujf-grenoble.fr).

amendments with municipal waste and animal manures, or ground rubber) and industrial activities such as atmospheric fallout from smelters (Adriano, 1986; Chaney, 1993). Second, and foremost, zinc may be taken up by a large number of organic and inorganic soil constituents in both oxic and anoxic environments owing to its high chemical affinity for both oxygen and sulfur ligands, and its ability to easily switch from tetrahedral to octahedral coordination. Zn effective ionic radii differ by < 10% from those of  ${}^{\text{VI}}\text{Al}^{3+}$  (0.53 Å) and  ${}^{\text{VI}}\text{Fe}^{3+}$  (0.64 Å) in fourfold coordination (0.60 Å for  ${}^{\text{IV}}\text{Zn}^{2+}$ ), and from those of  ${}^{\text{VI}}\text{Mg}^{2+}$  (0.72 Å) and  ${}^{\text{VI}}\text{Fe}^{2+}$  (0.78 Å) in sixfold coordination (0.74 Å for  ${}^{\text{VI}}\text{Zn}^{2+}$ ), thus providing a rationale for its possible incorporation in a large number of soil minerals.

The complex mixture of inorganic, and to a lesser extent organic, Zn species may be resolved using an array of analytical techniques (SEM, PIXE, SXRF, XRD, etc.), and physical (size and densimetric separation) and chemical (selective dissolution) fractionation as an adjunct to extended X-ray absorption fine structure (EXAFS) spectroscopy (Manceau et al., 2000a; Hansel et al., 2001; Isaure et al., 2002; Roberts et al., 2002; Scheinost et al., 2002). Since an EXAFS spectrum is a weighted sum of spectra from all species present in the analyzed volume (Manceau et al., 1996), fractionating the sample can help in identifying individual species in two ways: first, by reducing the number of component species in each weighted spectrum and, second, by maximizing the number of observables in recording as many distinct EXAFS spectra as there are soil fractions. Another way to vary the proportions of the species in any single spectrum is to take  $\mu\text{EXAFS}$  spectra at different spots in the unperturbed sample, making use of the micrometer-scale heterogeneity of environmental materials. This approach is preferable because chemical extractions can cause artifacts (Ostergren et al., 1999), and because micrometer-scale areas generally contain only one to three species, thereby facilitating their identification (i.e., the system is better constrained). However, this latter approach requires the use of a state-of-the-art X-ray microscope, whose number and accessibility worldwide is limited. Once the system is over-determined, that is when more distinctly different EXAFS spectra than unknowns have been collected, then the number and nature of individual species can be rigorously evaluated by principal component analysis (PCA) (Ressler et al., 2000). Then, species proportions in the bulk material are estimated by least-squares fitting (LSF) the EXAFS spectrum of the powdered sample to the combination of component spectra previously identified by PCA. Still, PCA is a statistical treatment of a set of mixed spectra, and this quantification procedure requires that all individual species are either present in a reference database or, preferably, that their spectra were recorded by  $\mu\text{EXAFS}$ . Ideally, one would want to record at least as many single-component  $\mu\text{EXAFS}$  spectra as there are metal species in the heterogeneous matrix. This is generally possible for coarse-grained primary minerals, but less so for finely-divided secondary minerals (e.g., phyllosilicates, Fe and Mn [oxyhydr]-oxides, etc.) because in most cases they are mixed at the micrometer scale.

One way to avoid this difficulty, or at least to reduce any guesswork and strengthen the degree of certainty of the metal species identification, is to complement the  $\mu\text{EXAFS}$  analysis by synchrotron-based X-ray micro-fluorescence ( $\mu\text{SXRF}$ ) and

micro-diffraction ( $\mu\text{XRD}$ ) (Manceau et al., 2002b, 2002c).  $\mu\text{SXRF}$  is used first to map the distribution of elements within the heterogeneous matrix. After trace and major elements have been located within the matrix,  $\mu\text{XRD}$  is used to identify the nature of the likely minerals hosting a particular trace element. Finally, with  $\mu\text{EXAFS}$  spectroscopy, the molecular-scale incorporation mechanism of the metal within the mineral host is determined (i.e., the true species is identified).

The potential of this novel three-pronged analytical approach, which is being developed at the Advanced Light Source (ALS), is demonstrated here by determining the Zn species in the solid phases of a single sample from a pristine horizon of a clayey soil. Under the optical microscope, the sample exhibits a heterogeneous fabric, with traces of localized manganiferous, ferriferous and argillaceous accumulations. The presence of the localized accumulations increases the possibility of collecting Zn-EXAFS spectra from only one or two species and, hence, of detecting new Zn species or confirming the existence of others proposed from published least-squares fits of multi-component EXAFS spectra.

## 2. MATERIALS AND METHODS

### 2.1. Soil Sample

The studied sample comes from a cultivated soil of a Weinbach series (Aeric Fragiaguult) occurring on a high terrace of the Ohio River. This soil is located about two km west of the soil hydrosequence described by Smeck et al. (2002). It is characterized by an acidic pH (4.5–5.0) and a fragipan (Btx) horizon at ~80 to 130 cm rich in siltans and mangans and saturated in water for ~20% of the time. A mottle of ~6 cm in diameter was taken at the top of the fragipan horizon. A fragment of the mottle was dried at 80°C overnight in an oven, then impregnated with Scotchcast epoxy (3M company), a high purity resin, and a thin section mounted on a quartz slide was prepared. LR White resin (SPI Supplies, West Chester, PA) was not used because it has been reported to oxidize As(III) to As(V) (Strawn et al., 2002) and, therefore, may not be inert with respect to the Mn oxidation state.

Petrographic observation with transmitted light showed Fe- and Mn-enrichments expressed as individual reddish grains and reddish to blackish diffuse strips cementing the fine clay matrix, while the highest clay concentrations occurred as pore infillings. In humid temperate climates, these pedological traits are observed typically in hydromorphic soils, particularly in soils with impeded internal drainage (Hseu and Chen, 1997, 1999). In these soils, Fe and Mn are partly reduced and mobilized during the wetter season and precipitated and concentrated during the drier season in various forms, among which mottles and concretions are the most frequent. The extensive deposition of fine clay particles in pores (siltans), which results from downward transport and accumulation where flow is restricted, is also indicative of periodic change in soil moisture status. Another fragment of the mottle was air dried, ground, acid-digested, and analyzed by inductively coupled plasma atomic emission spectroscopy (ICP-AES) for major element concentrations and by inductively coupled plasma mass spectroscopy (ICP-MS) for trace element concentrations. Results (Table 1) show that the sample composition is dominated by Si ([SiO<sub>2</sub>] = 60.3 wt.%), Al ([Al<sub>2</sub>O<sub>3</sub>] = 12.2 wt.%), Fe ([Fe<sub>2</sub>O<sub>3</sub>] = 13.2 wt.%), and to some extent by Mn ([MnO] = 1.69%) which ordinarily comprises < 1% of the total soil material. The most abundant trace elements are Ba (457 mg/kg), Zr (313 mg/kg), Ce (134 mg/kg), Zn (128 mg/kg), and Co (107 mg/kg). Nickel (43 mg/kg), lead (64 mg/kg) and all other trace element amounted to < 100 ppm.

### 2.2. Methods

The bulk mineralogy of the <0.2- $\mu\text{m}$  clay fraction was investigated using X-ray diffraction on samples treated with organic liquids (glycerol, G, and ethylene glycol, EG) and heat. The <0.2- $\mu\text{m}$  fraction was separated from the <2- $\mu\text{m}$  fraction by centrifugation at 4000 rpm for

Table 1. Chemical analysis.

	Weight percent (%)
SiO <sub>2</sub>	60.3
Fe <sub>2</sub> O <sub>3</sub>	13.2
Al <sub>2</sub> O <sub>3</sub>	12.2
MnO	1.69
K <sub>2</sub> O	1.66
TiO <sub>2</sub>	0.76
MgO	0.65
Na <sub>2</sub> O	0.60
P <sub>2</sub> O <sub>5</sub>	0.30
CaO	0.15
Weight loss at 1000°C	8.21
Total	99.7

25 min, and the <2- $\mu\text{m}$  fraction by centrifugation at 700 rpm for 8 min of the <2-mm soil fraction decarbonated overnight with buffered (pH 5) sodium acetate solution. After size-fractionation, the clay separate was saturated with either Mg in 0.5 mol/L MgCl<sub>2</sub> for G and EG saturation, or K in 1.0 mol/L KCl for heat treatment. Suspensions were shaken in the saline solutions for a minimum of 12 h, and the exchange was repeated twice to ensure a complete removal of exchangeable interlayer cations. Excess chloride was rinsed out by centrifugation. Oriented preparations of the homoionic clay fractions were prepared by pipetting a clay slurry onto a glass slide and drying it at room temperature. Glycerol solvation was achieved by pressing the oriented slides on glycerol-soaked filter paper. Excess liquid glycerol was removed by pressing the wet slide onto dry paper. Ethylene glycol saturation was performed by leaving an oriented mount on the shelf of an EG-containing desiccator placed overnight in oven at 60°C. XRD patterns were recorded with a Bruker D5000 diffractometer equipped with a Cu anode and a Kevex Si(Li) solid state detector, and using a 0.02° step size and 12-s counting time per step. An Anton Paar TTK450 chamber coupled to an Asynco humidity controller was used to record the room temperature XRD patterns at constant relative humidity (~40% RH). Oriented slides of the K-saturated clay fraction were heated *ex situ* for 2 h at 100, 300, and 550°C, before XRD data collection.

X-ray microscopic measurements were performed at the Advanced Light Source (Berkeley) on 10.3.2 ( $\mu\text{SXRF}$  and  $\mu\text{EXAFS}$ ) and 7.3.3 ( $\mu\text{XRD}$ ) stations using a set-up similar to that used in previous studies (Manceau et al., 2002c). For  $\mu\text{SXRF}$  measurements, two areas with dimensions of 3 mm (horizontal)  $\times$  6 mm (vertical) and 4.5 mm (H)  $\times$  7 mm (V) were scanned under the monochromatic beam at  $E = 10$  keV with steps of 20  $\mu\text{m}$  and 100-ms dwell time. Mn- and Zn-K edge  $\mu\text{EXAFS}$  spectra were collected at various points-of-interest (POIs). Multiple spectral scans, totaling from 30 s/point for the most concentrated spots up to 230 s/point for the most diluted spots, were performed to yield high signal-to-noise (S/N) ratio  $\mu\text{EXAFS}$  spectra ( $4 \times 10^6$  to  $12 \times 10^6$  total Mn/Zn K $\alpha$  counts, depending on the amplitude of the EXAFS oscillations). For  $\mu\text{XRD}$  experiments, POIs were relocated using  $\mu\text{SXRF}$  and then point XRD patterns were collected in reflection geometry with a photon energy of 6 keV, a beam size on the sample of 15  $\mu\text{m}$  H  $\times$  20  $\mu\text{m}$  V, and a 1024  $\times$  1024 pixels CCD camera for the detection of the diffracted beam. The FAME spectrometer at the European Synchrotron Radiation Facility (ESRF, BM30B) was used to collect the average Zn K-edge EXAFS spectrum from a powder of a mottle. EXAFS data were normalized and least-squares fitted to a combination of reference spectra using home-made software. Linear combinations of model spectra were optimized by minimizing the Sum-sq parameter defined as the sum of the squares of the residuals, normalized to the sum of the squares of the data values. The only adjustable parameters were the fractions of each model compound contributing to the fit. Three new reference spectra were added to our extensive database of Zn spectra described previously (Manceau et al., 2003): Zn-doped ("Zn-copr. HIM") and Zn-sorbed ("Zn-sorbed HIM") hydroxy-interlayered montmorillonite spectra from Scheinost et al. (2002), and Zn-sorbed gibbsite from Roberts et al. (2003).

### 3. RESULTS

#### 3.1. XRD Analysis of the Fine Clay Fraction

The mineralogy of the <0.2- $\mu\text{m}$ -size fraction is dominated by illite/mica (d-spacings of 10.0, 5.00, and 3.34 Å), kaolinite (d-spacings of 7.14, and 3.57 Å), and expandable minerals (Fig. 1a). Lepidocrocite is also present as a major accessory mineral whereas only traces of quartz are detected. In the air-dried state, Mg-saturated expandable minerals are characterized by the presence of a peak at 14.2 Å, which is asymmetric towards higher angles (black arrow). Upon glycerol and ethylene glycol solvation, the scattering tail disappears resulting either in a single peak at 14.2 Å (G) or a peak at 14.2 Å plus a broad feature at 16 to 18 Å (EG). For Mg-saturated clays, this behavior is characteristic of vermiculite and contrasts with that of smectite, which expands with both G and EG (Malla and Douglas, 1987; Douglas, 1989; Moore and Reynolds, 1997). These expandable layers do not collapse spontaneously to 10.2 Å after K-saturation and gentle heating (Fig. 1b). Instead, they remain expanded to temperatures > 100°C, and collapse only partly at higher temperatures (~11.6 Å above 300°C). This thermal behavior arises from hydroxy-Al interlayers (Douglas, 1989; Moore and Reynolds, 1997), which compensate partially the charge deficit of the vermiculite layers. This hydroxy species is commonly encountered in aluminum-rich acidic clayey soils with restricted drainage (Chen et al., 2001; Marques et al., 2002). Lepidocrocite, which transforms to maghemite between 100 and 300°C, and kaolinite, which dehydroxylates below 550°C, exhibit standard thermal behaviors (Fig. 1b).

#### 3.2. $\mu\text{SXRF}$

Two-color (Green-Blue) and tricolor (Red-Green-Blue) maps of the distribution of Fe (green), Mn (blue), and Zn (red) are presented in Figure 2. The relatively pure green and blue color of the Mn- and Fe-rich area in the two-color representation indicates that Fe and Mn are at the same time highly segregated but uncorrelated, as commonly observed at every probed scale in environmental materials. The dim greenish cast of the argillaceous matrix indicates that the whole soil plasma body is in fact permeated with iron, but in an amount which greatly varies from one place to another. Since ferriferous and manganiferous segregation in soils occurs as a result of pedogenic processes that accumulate elements by chemical and biologic actions (Singh and Gilkes, 1996), the uneven distribution of Fe and Mn often yields a differentiated fabric whose pattern may provide insight on the current or relic dynamics of soil processes (Brewer, 1976; FitzPatrick, 1993). In the present case, Mn and Fe often form subconcentric laminae around voids partly or totally infilled with clayey material. The upper left regions of Figures 2a and 2b show two typical examples of a still incompletely filled void, whereas the two intermeshed globules in the center of the first map may correspond to old voids. The two distinct Mn laminae which delineate the original contour of the unfilled void in Figure 2b may indicate formation in waves during alternating wet and dry periods with desiccation formation of each lamina. Some voids are delineated with Fe or Mn sesquioxides and others not. The first type likely corresponds to old root plaques, which persisted after the decomposition of organic matter (Hansel et al., 2001).

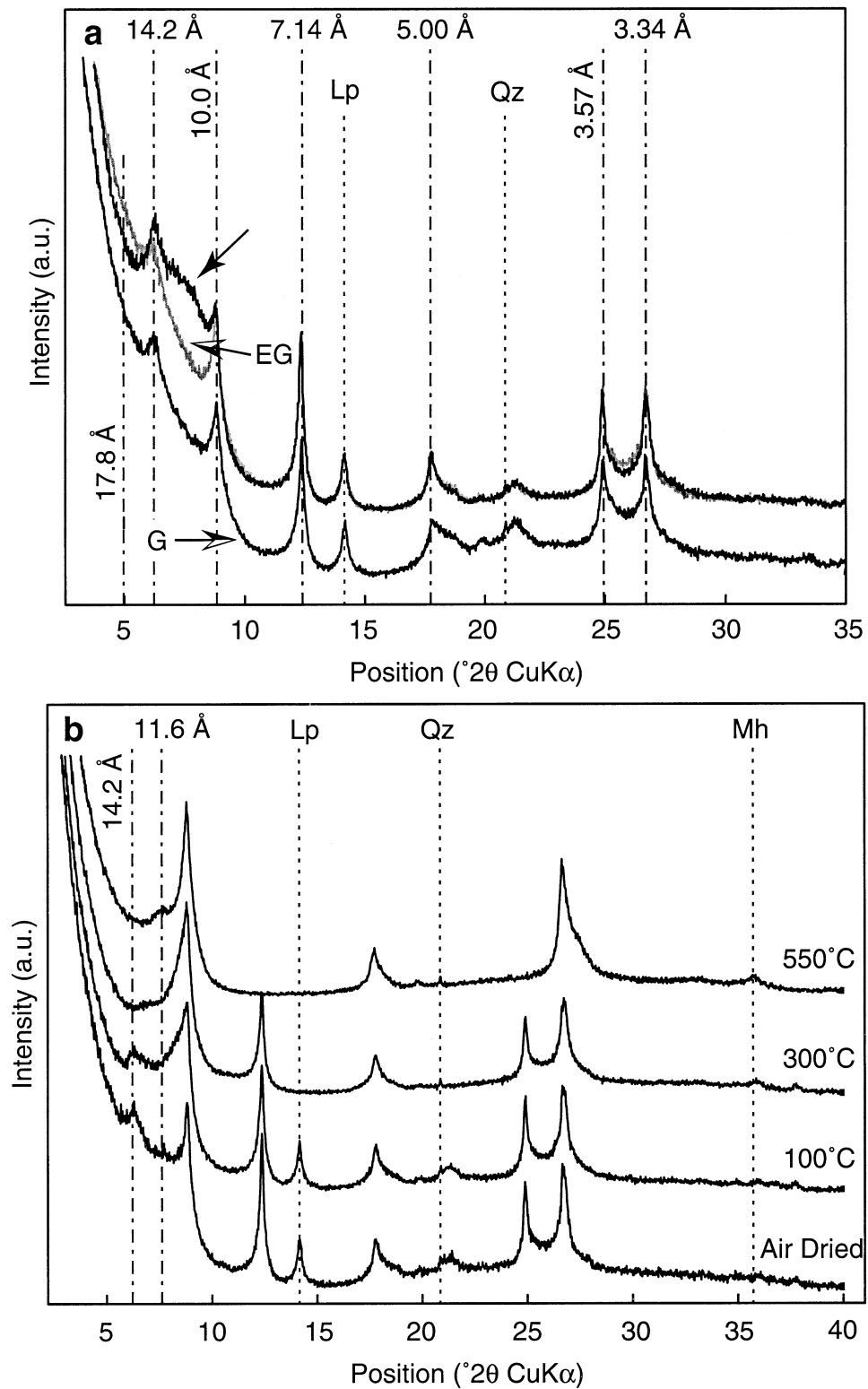


Fig. 1. X-ray diffraction patterns collected on oriented preparations of the  $<0.2\text{-}\mu\text{m}$ -size fraction. (a) Mg-saturated mount in the air-dried state (black line) and after ethylene glycol (grey line, EG curve) and glycerol (black line, G curve) solvation. (b) K-saturated mount after *ex situ* thermal treatment. Dashed lines show the positions of non-phyllsilicates phases (Lp: lepidocrocite; Qz: quartz; Mh: maghemite), and dot-dashed lines those of layer silicates.

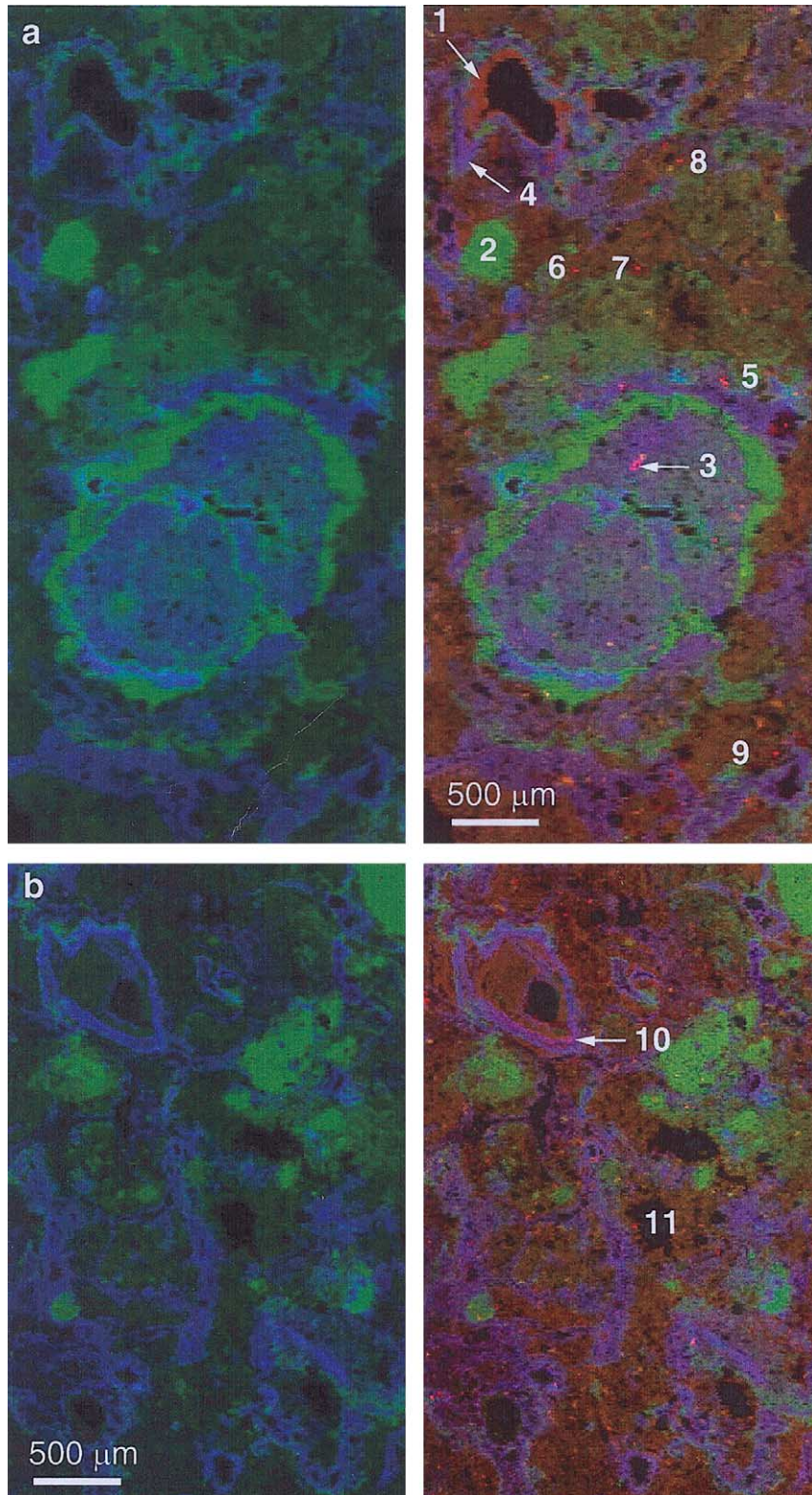


Fig. 2. Two-color (GB) and tricolor (RGB) maps of the distribution of Fe (green), Mn (blue), and Zn (red) in the soil mottle. The intensity of each color in each pixel is proportional to the amount of the corresponding element. The overall brightness of a region is related to the sum of the concentrations, and the hue is related to the ratio. Zn is present everywhere in the argillaceous matrix as indicated by the brownish cast of the two RGB maps. The green patches are goethite, the red hot spots are sphalerite ( $ZnS$ ) and zincochromite ( $ZnCr_2O_4$ ) grains, and the pink elongated grain in (a) is lithiophorite. The matrix contains argillans and mangans, which are indicative of downward transport (eluviation) and accumulative deposition where flow was restricted (illuviation). The analyzed spots are indicated by numerical values.

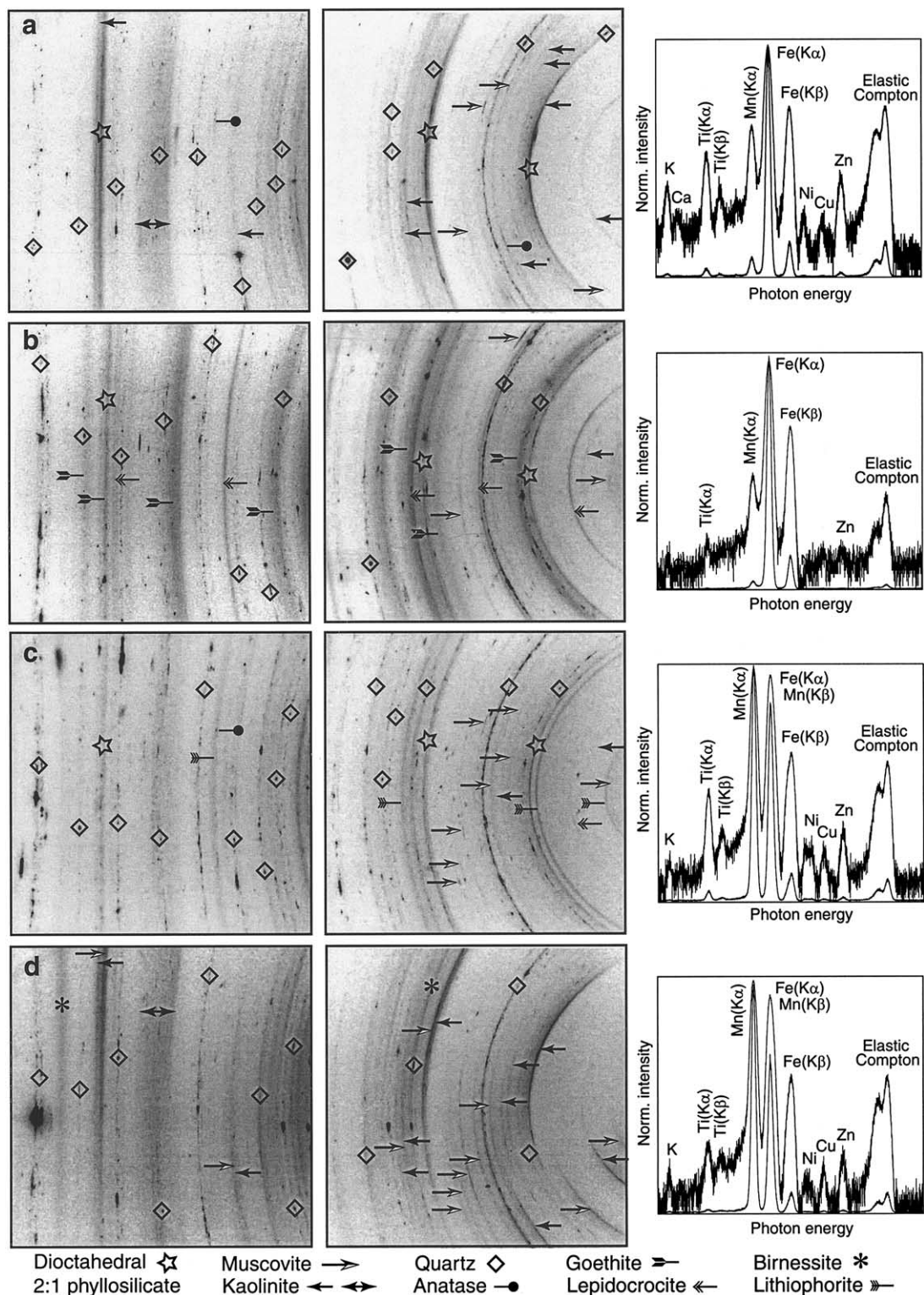


Fig. 3. Two-dimensional  $\mu$ XRD patterns ( $\lambda = 2.066 \text{ \AA}$ ) and X-ray fluorescence spectra (linear and log scale) collected in points P-1 (a), P-2 (b), P-3 (c) and P-10 (d) from the elemental maps presented in Figure 2. Diffractograms on the right have  $1.94 \text{ \AA} < d(hkl) < 13.0 \text{ \AA}$ , and those on the left have  $1.33 \text{ \AA} < d(hkl) < 2.49 \text{ \AA}$ .

Zinc is present everywhere in the argillaceous matrix as indicated by the brownish cast of the two RGB maps. Apart from the cutan in the top left of Figure 2a, whose reddish color

indicates a higher Zn content, the almost uniform cast of the matrix indicates that Zn concentration is relatively homogeneous within the clayey matrix. The purple (mix of blue and

red) coloring of the inner Mn laminae in the void of Figure 2b reveals the presence of Zn. A few other Zn-Mn associations in well-defined hot-spots relative to surrounding areas are also clearly visible, with the biggest grain of  $\sim 50 \times 100 \mu\text{m}$  in size being observed inside the Fe-Mn globule (point labeled 3). The third Zn pool is represented by few micrometer-sized Zn-rich grains showing as bright red and distributed throughout the soil matrix. Note that Fe-rich, as well as most Mn-rich regions, contain little zinc.

### 3.3. $\mu\text{XRD}$

From visual inspection of the two elemental maps presented previously, a dozen POIs were selected for  $\mu\text{XRD}$  measurements. Figure 3 shows a selection of four representative two-dimensional diffraction patterns collected at points P-1, P-2, P-3 and P-10 (Figs. 3a–3d, respectively) together with the energy-dispersive X-ray fluorescence spectra at the same points. Two-dimensional XRD patterns show continuous to discontinuous or spotty diffraction rings arising from a range of nanometer- to submicrometer-sized crystallites. Fine particles include phyllosilicate, goethite, lepidocrocite, lithiophorite, and turbostratic birnessite (vernadite), and silty to coarse particles are quartz, feldspar and anatase. Lepidocrocite was identified also in the nearby soil hydrosequence studied by Smeck et al. (2002), and is regarded as an indicator of humidity because it normally forms in hydromorphic soils by oxidation of  $\text{Fe}^{2+}$  in the soil solution (Schwertmann and Taylor, 1989). Phyllosilicate is by far the most abundant family of minerals with 2:1 (illite/mica, vermiculite) and 1:1 (kaolinite) Al clays being the two predominant species observed everywhere in variable proportions and admixtures with other minerals. The highest amounts of 2:1 phyllosilicate and kaolinite were detected in the ferriargillan void (cutan) of Figure 2a as indicated by the overwhelming intensity of the  $hk0$  reflections at 4.48, 2.57, 1.50 (dioctahedral smectite) and 1.49 Å (kaolinite). The 2:1 phyllosilicates are the main repositories for the alkali ( $[\text{Na}_2\text{O}] = 0.60 \text{ wt.}\%$ ;  $[\text{K}_2\text{O}] = 1.66 \text{ wt.}\%$ ) and alkaline earth ( $[\text{CaO}] = 0.15 \text{ wt.}\%$ ) metal ions measured by chemical analysis (Table 1). Micaceous minerals (peaks at  $\sim 10$  and  $5 \text{ Å}$ ) and 2:1 Fe clays (peak at 1.51–1.52 Å) were also identified in the argillaceous matrix, this latter species partly accounting for the diffuse distribution of Fe in the matrix. The intensity of the (001) and (002) reflections of kaolinite and micaceous phyllosilicate were either constant or moderately to extremely heterogeneous along the Debye rings, indicative of the existence of several populations of particles of different sizes. An example of a strongly textured XRD pattern exhibiting a partial  $\langle 001 \rangle^*$  fiber texture is presented in Figure 3d.  $\mu\text{XRD}$  patterns collected in the bright green Fe-rich areas of the SXRF maps identified goethite and lepidocrocite (Fig. 3b). Turbostratic hexagonal birnessite was detected systematically in Mn-rich regions from reflection maxima at 2.45 Å (100 reflection) and 1.41 to 1.42 Å (110 reflection). This mineral species assignment was confirmed by the strong correlation observed between the intensity of the 110 reflection and the Mn  $K\alpha$  fluorescence yield. XRD analysis of the Mn hot-spot in P-3 identified major lithiophorite in a mixture with phyllosilicate from the matrix.

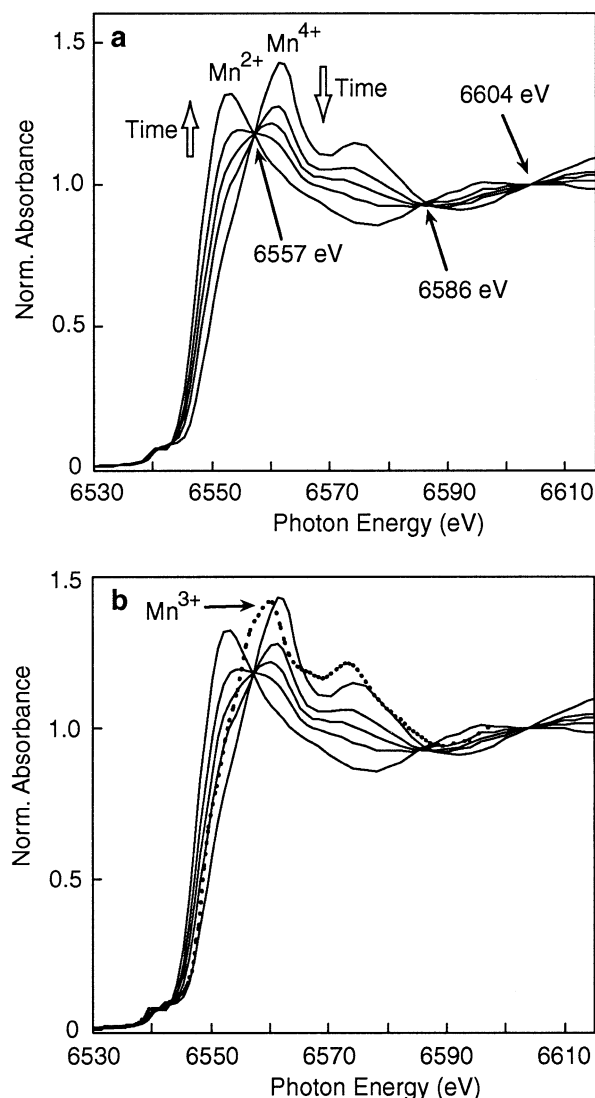


Fig. 4. (a) Characteristic time-dependent normalized Mn K-edge XANES spectra collected in a birnessite region. Manganese is completely photoreduced from the manganic to the manganous form after several hours of beam exposure. (b) The XANES spectrum of a  $\text{Mn}^{3+}$  reference ( $\gamma\text{-MnOOH}$ , dotted line) has been added to show that, if a transient  $\text{Mn}^{3+}$  species exists, its concentration should be low. The absolute energy of the spectra is calibrated to the first inflection point of elemental Mn (6539 eV).

### 3.4. Mn K-Edge $\mu\text{EXAFS}$

On the basis of  $\mu\text{XRD}$  results, three POIs were selected for Mn- $\mu\text{EXAFS}$  measurements, two in birnessite regions at points P-4 and P-10, and one on the lithiophorite grain at point P-3. Spectra collected in birnessite regions evolved with time due to radiation damage (Fig. 4a). The edge crest, which in the unperturbed state occurred at the characteristic  $\text{Mn}^{4+}$  value of 6561 to 6562 eV, progressively decreased in intensity, while a shoulder at  $\sim 6553 \text{ eV}$  characteristic of  $\text{Mn}^{2+}$  appeared and increased with time. Eventually, all the manganese was reduced from the manganic to the manganous form. The presence of isosbestic points (constant absorbance) at 6557, 6586, and 6604

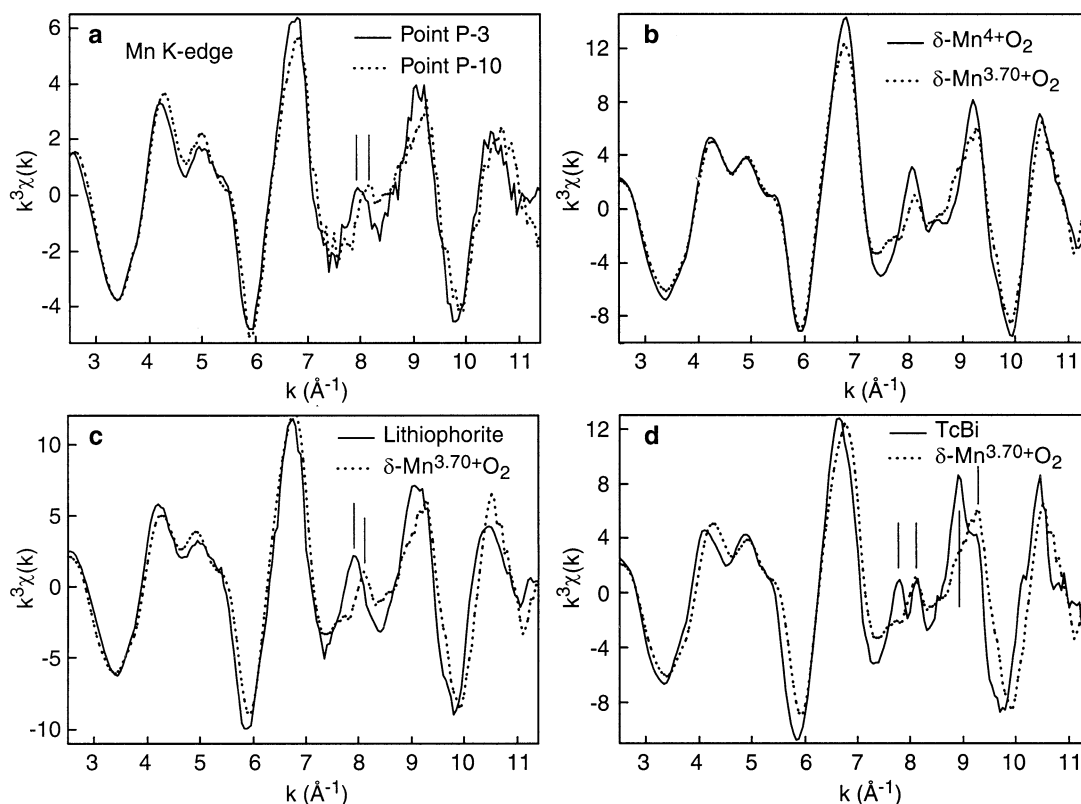


Fig. 5.  $k^3$ -weighted Mn-EXAFS spectra collected at points P-3 and P-10 (a) and from various phylломanganate references (b–d). The EXAFS spectrum of manganese in its unreduced form at point 10 was obtained by moving the sample by 30  $\mu\text{m}$  after each scan. (b) The  $\delta\text{-MnO}_2$  (solid line) and  $\delta\text{-Mn}^{3.70+\text{O}_2}$  (dotted line) references are from Villalobos et al. (2003). The exact amount of layer  $\text{Mn}^{3+}$  is unknown in  $\delta\text{-Mn}^{3.70+\text{O}_2}$  because  $\text{Mn}^{3+}$  cations are partly located in the interlayer region as in hexagonal birnessite (Hbi, Lanson et al., 2000). (c) The lithiophorite reference was synthesized according to the protocol by Yang and Wang (2003), and the mean oxidation state of Mn (3.68) was determined by potentiometric titration using  $(\text{NH}_4)_2\text{Fe}(\text{SO}_4)$  Mohr salt and sodium pyrophosphate (Vetter and Jaeger, 1966). (d) The synthetic triclinic birnessite reference is from Silvester et al. (1997).

eV indicates that the system is dominated by two components. If the X-ray induced photoreduction of  $\text{Mn}^{4+}$  to  $\text{Mn}^{2+}$  occurs by one-electron transfer, then the intermediate  $\text{Mn}^{3+}$  species should be present in low concentration. The fractional amount of this transient species cannot be high because its proportion should be constant over time (pseudobinary system) and in this case the XANES spectra of the  $\text{Mn}^{4+}$  and  $\text{Mn}^{2+}$  end-members should be multi-component spectra (Fig. 4b). The reduction of Mn(IV) to Mn(II) in soils upon X-ray radiation was reported by Ross et al. (2001), who contended that the source of electrons for the photoreduction was soil organic molecules. This hypothesis is consistent with the possible biogenic origin of our soil birnessite, with laboratory observations which showed that biogenic Mn precipitates are in close contact with the cell surface and exopolymers (Tebbo et al., 1997), and with the concentration of organic carbon in the fragipan horizon (3–4 g/kg; Smeck et al., 2002). Another possible source of electron for the photoreduction of manganese is the resin used for embedding. To alleviate this problem, each spectrum was collected in a shorter time and the sample was moved by 30  $\mu\text{m}$  around point P-4 and along the manganese lamina of P-10 to analyze a new spot every other scan. Then, these individual

spectra were carefully scrutinized for possible reduction effects before summation.

The two birnessite EXAFS spectra collected at points P-4 and P-10 were superimposable over the whole experimental  $k$  range, meaning that Mn is, on average, in the same form in the two analyzed spots. The soil birnessite (P-4, P-10) and lithiophorite (P-3) spectra are essentially the same, except in the 7 to 10  $\text{\AA}^{-1}$  interval (Fig. 5a). Meticulous data analysis by Fourier filtering experimental spectra, ab initio FEFF calculation (Mestre de Leon et al., 1991) from structural models, and comparison to phylломanganate and tectomanganate references led us to conclude that the two soil manganates have a layered structure built of edge-sharing Mn octahedra with no detectable interlayer Mn atoms (i.e., no corner-sharing Mn octahedra). During this detailed spectral analysis, our attention was drawn by the subtle, but meaningful, variation of the spectral shape between 7 and 10  $\text{\AA}^{-1}$ , especially among the phylломanganate series of minerals (Figs. 5b–5d). A clear relationship could be established between the position (i.e., electronic wave frequency) and shape of the two wave resonances in this  $k$  interval and the presence and distribution of trivalent Mn atoms in the manganese layer. In the absence of layer  $\text{Mn}^{3+}$ , as in stoichi-

ometric  $\delta\text{-MnO}_2$  (Villalobos et al., 2003), the two resonances are intense and symmetrical, and peak at 8.05 and 9.2  $\text{\AA}^{-1}$ . In  $\delta\text{-Mn}^{3.70+}\text{O}_2$  (Villalobos et al., 2003), the positions are preserved, but the amplitudes are lower and the peaks are broadened on their left side. When the amount of layer  $\text{Mn}^{3+}$  is higher, the two resonances shift to 7.9 and 9.0  $\text{\AA}^{-1}$  as in synthetic lithiophorite ( $\text{Mn}^{3+}/\text{Mn}^{4+} = 0.47$ ; Yang and Wang, 2003), or the first resonance is split into two maxima at 7.8 and 8.1  $\text{\AA}^{-1}$  and the second is shifted to 8.9  $\text{\AA}^{-1}$  as in synthetic triclinic birnessite ( $\text{TcBi}$ ,  $\text{Na}_{0.30}\text{Mn}_{0.05}^{2+}[\text{Mn}_{0.74}^{4+}\text{Mn}_{0.21}^{3+}\square_{0.05}]\text{O} \sim 2$ , Silvester et al., 1997). The left-shift in frequency observed in  $\text{Mn}^{3+}$ -containing phyllosulfates is indicative of higher interatomic distances, and is consistent with the bigger size of  $\text{Mn}^{3+}$  relative to  $\text{Mn}^{4+}$  cations. FEFF simulations showed that the atomic shell at play here is the first Mn shell, which is at  $b \sim 2.84$   $\text{\AA}$  from the central atom (i.e., X-ray absorber) in pure  $\text{Mn}^{4+}$  layers (Manceau et al., 1997; Lanson et al., 2000) and at  $b = 2.925$   $\text{\AA}$  in lithiophorite (Post and Appleman, 1994). In  $\text{TcBi}$ ,  $\text{Mn}^{3+}$  cations are segregated in rows along the [010] direction that are separated by two  $\text{Mn}^{4+}$  rows along the [100] direction (Drits et al., 1997; Lanson et al., 2000). Owing to the ordering of Mn atoms and the Jahn-Teller distortion of the  $\text{Mn}^{3+}$  octahedra, the nearest Mn shell is split into two subshells of 2 Mn at 2.85  $\text{\AA}$  and 4 Mn at 2.95  $\text{\AA}$  (Lanson et al., 2002). This shell splitting is responsible for the node pattern at 7.8 to 8.1  $\text{\AA}^{-1}$  but not for its depth at 7.95  $\text{\AA}^{-1}$ . In fact, data analysis showed that the node is blunted whenever the intense Mn higher shell contribution at  $\sim 2.90 \times 3 = 8.7$   $\text{\AA}$  is suppressed from the whole EXAFS spectrum of  $\text{TcBi}$  because the electronic wave for this shell has a maximum amplitude at 7.8 and 8.1  $\text{\AA}^{-1}$  and a minimum (i.e., the amplitude is negative) at 7.95  $\text{\AA}^{-1}$ . In conclusion, detailed analysis of the EXAFS spectra of phyllosulfate references shows that the spectral shape in the 7.0 to 10.0  $\text{\AA}^{-1}$  interval is sensitive to the amount and ordering of  $\text{Mn}^{3+}$  cations in the octahedral layer, thereby allowing characterization of the nature and stoichiometry of unknown phyllosulfate. In the present study, this spectral indicator confirms that the two phyllosulfates identified by X-ray microdiffraction at points P-4 and P-10, and at point P-3, are vernadite-like  $\text{Mn}^{3+}$ -containing birnessite and lithiophorite, respectively. Our mineral species assignment is further confirmed by the direct comparison of the two soil spectra with the two reference spectra (Fig. 6).

### 3.5. Zn K-Edge $\mu\text{EXAFS}$

Energy-dispersive fluorescence spectra (XRF) and  $\mu\text{EXAFS}$  spectra of the Zn-rich grains P-5 to P-9 and P-11 in Figure 2 were recorded first, and a selection of results is presented in Figure 7. Apart from P-5, all the analyzed grains were extremely rich in Fe and Zn, and their EXAFS spectra and radial structure functions (RSFs) were found to be the same as ZnS (Figs. 8a and 8b). A revealing characteristic of the RSF for POI P-5 is the low distance shift of the first shell peak to a position typical of a metal coordinated to oxygens (Fig. 7d). The best spectral agreement between the unknown species and spectra from our extended library of Zn model compounds was obtained with franklinite ( $\text{ZnFe}_2\text{O}_4$ ), a species previously identified in soils (Fig. 8c) (Manceau et al., 2000a; Roberts et al., 2002). The unknown and known spectra have about the same

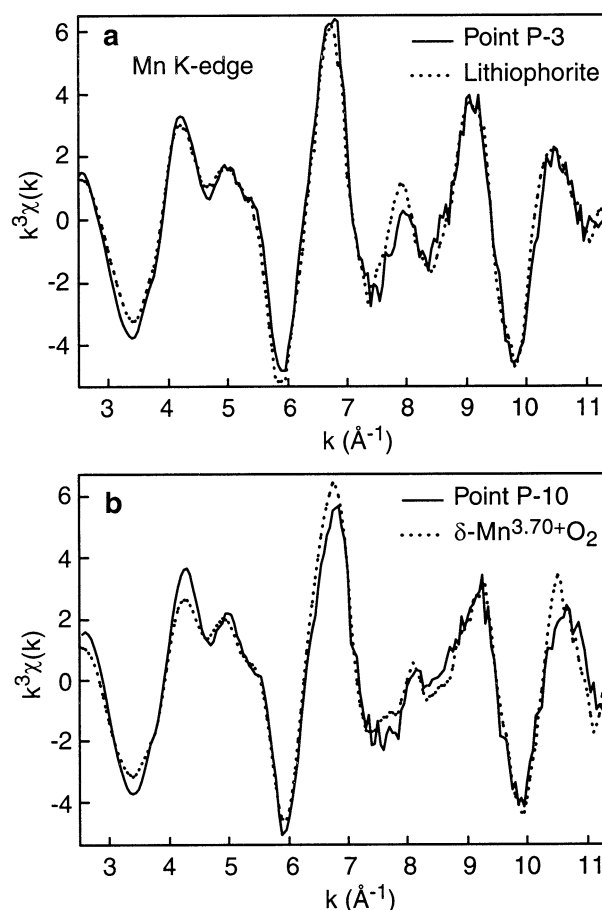


Fig. 6. Best one-component spectral fit between the soil Mn-EXAFS spectra at points P-3 and P-10 and the reference spectra for Mn oxides. The amplitude of the two reference spectra was multiplied by 0.51 to account for self-absorption effects in the measurement of the soil spectra in fluorescence detection mode (Manceau et al., 2002b).

spectral shape but a different frequency, with the former spectrum being shifted to higher  $k$  values. These spectral likenesses and differences indicate that the two Zn minerals have the same framework structure but that the unknown species has shorter interatomic distances around Zn. Since energy dispersive analysis shows that this grain contains Cr as well as Fe and Zn, and since  $\text{Cr}^{3+}$  has a smaller size than  $\text{Fe}^{3+}$  (0.61 vs. 0.64  $\text{\AA}$ ), Zn is likely speciated as  $\text{Zn}(\text{Cr},\text{Fe})_2\text{O}_4$ . The Cr/Zn stoichiometry can be evaluated from the relative intensity of the Cr and Zn  $\text{K}\alpha$  fluorescence lines in the energy dispersive spectrum after correction of matrix absorption and Cr and Zn fluorescence yield effects. This calculation yielded a Cr/Zn ratio of about two, leading to the conclusion that this Zn grain consists of zincchromite ( $\text{ZnCr}_2\text{O}_4$ ; Nesterov and Rumyantseva, 1987). In keeping with this phase attribution, the comparison of the Fourier transforms for  $\text{ZnFe}_2\text{O}_4$  and the presumed  $\text{ZnCr}_2\text{O}_4$  species shows that the two compounds have the same Zn-O distance (Zn is tetrahedrally coordinated in the two inverse spinel structures), but that the Zn-Cr shells (second and higher distance RSF peaks) are slightly, but systematically, shortened in the soil grain owing to steric effects (Fig. 8d).

In an effort to strengthen our mineral phase assignment,

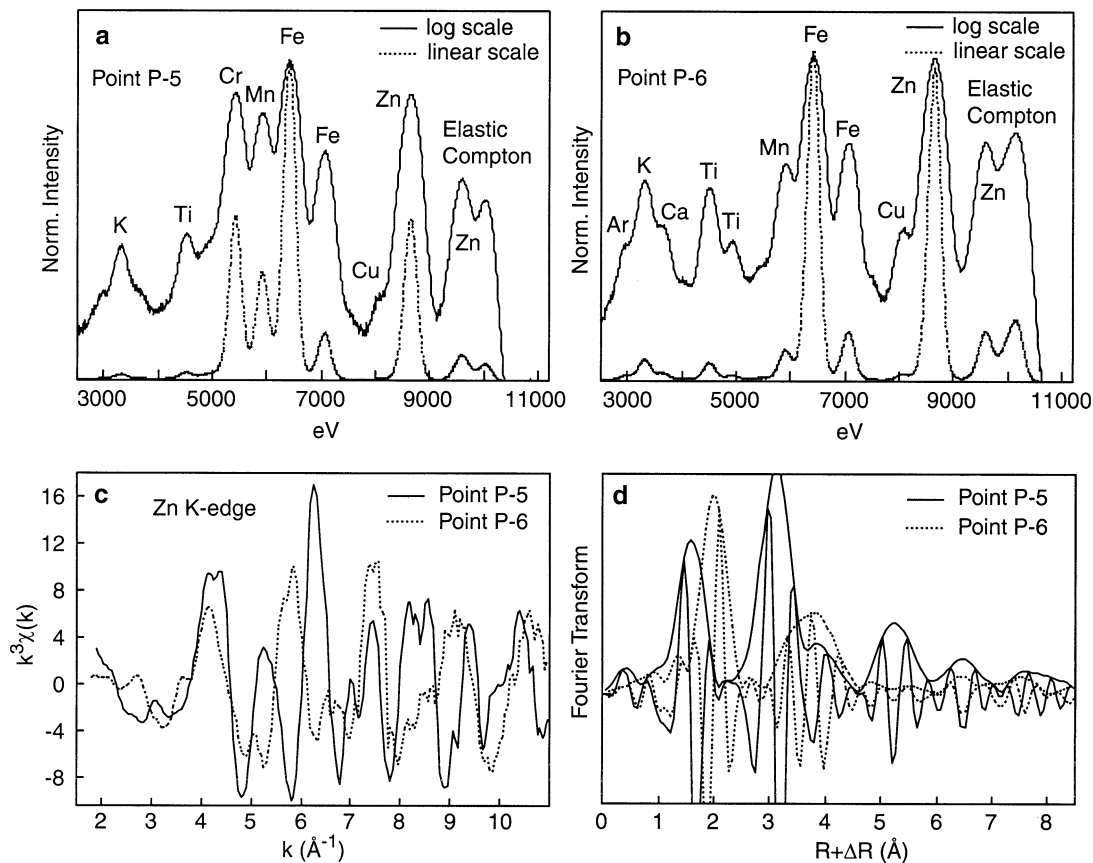


Fig. 7. Typical X-ray fluorescence spectra (a, b),  $k^3$ -weighted Zn-EXAFS spectra (c), and radial structure functions (d) obtained from the analysis of Zn hot spots in Figure 2.

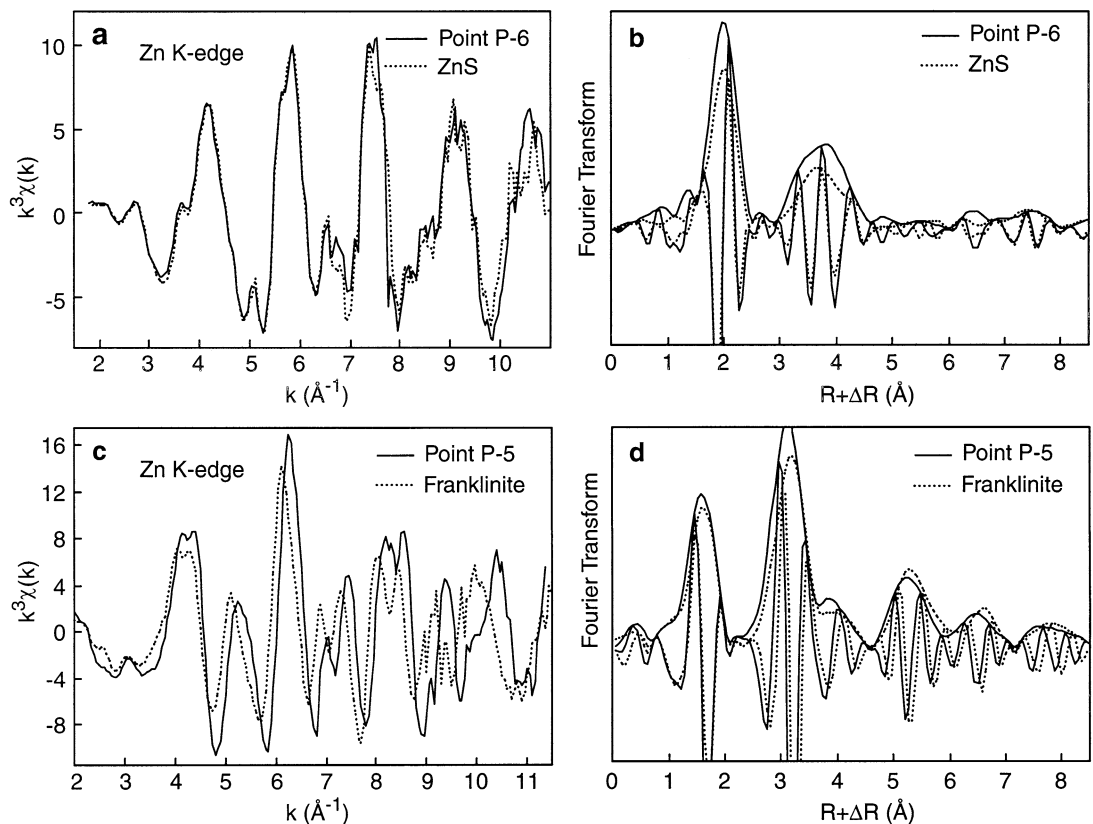


Fig. 8. Comparison of the two types of  $k^3$ -weighted Zn-EXAFS spectra and radial structure functions obtained from the analysis of Zn hot spots with data from Zn reference compounds. The micrometer-sized Zn-rich grains dispersed throughout the soil matrix consist of sphalerite (ZnS) and zincochromite ( $\text{ZnCr}_2\text{O}_4$ ). The amplitude of the EXAFS spectrum for the ZnS reference has been multiplied by 1.36 to account for the reduced amplitude of the experimental spectrum due to self-absorption effect (Manceau et al., 2002b).

theoretical EXAFS spectra for gahnite ( $\text{ZnAl}_2\text{O}_4$ ), franklinite and zincochromite were calculated by ab initio full multiple X-ray scattering calculation using the FEFF 7.02 code (Mustre de Leon et al., 1991) and the crystal structure of these minerals determined by X-ray diffraction (O'Neill and Dollase, 1994; Sepelak et al., 1996; Sawada, 1997). The calculations were carried out using a minimum number of parameters and by setting them to typical values for mineral structures (O'Day et al., 1994; Manceau et al., 1998). The amplitude reduction factor,  $S_0^2$ , was set to 0.85,  $R_{\text{max}}$  to 9 Å, NLEG to 4 (up to four successive scattering paths with total distances 9 Å were evaluated), paths falling below a cut-off in magnitude of 6% of the mean amplitude of the first Zn-O shell were excluded, and Debye-Waller factors were set to 0.06 Å for the nearest O shell, 0.08 Å for the two-nearest cationic shells, and to 0.1 Å for all higher shells and multiple scattering (MS) paths. Only the calculated energies were adjusted in the calculations and shifted + 4 eV to give best agreement with experiment. Figures 9a and 9b show that the spectral differences between the three zinc spinels are extremely well reproduced by the calculation. In particular, the shape of the  $\text{ZnCr}_2\text{O}_4$  spectrum is akin to that of  $\text{ZnFe}_2\text{O}_4$  but is right-shifted in wavenumber because the two spinels have exactly the same structure (Cr and Fe have the same coordinates) and only differ by their unit-cell  $a$  parameter ( $a = 8.3267$  vs.  $8.4432$  Å, respectively). The difference in phase and shape of the gahnite spectrum illustrates the sensitivity of EXAFS to the chemical composition of the spinel, and allows us to reject the presence of aluminum in the zincochromite phase. Finally, Figure 9c shows that there is an excellent agreement between theory and data for  $\text{ZnCr}_2\text{O}_4$ , especially if one keeps in mind that only the threshold energy of the free electron was adjusted in the calculation ( $\Delta E$ ), and that its value was treated as a single adjustable parameter for all sets of backscattering atoms and paths.

The nature of Zn-containing secondary mineral species was probed by recording Zn-EXAFS spectra at POIs P-1, P-3 and P-10. The three  $\mu\text{EXAFS}$  spectra are markedly different, and close examination shows that none of them can be reconstructed by a linear combination of the two others (Fig. 10a). A distinctive feature of spectra P-1 and P-3 is the peak doublet at 3.5 to 4.1 Å<sup>-1</sup>, which is systematically observed when Zn is octahedrally coordinated and shares edges with Mg or Al octahedra as in phyllosilicate, lithiophorite, gibbsite and hydroxy-Al interlayers (Manceau et al., 1987, 2000b; Roberts et al., 2002; Scheinost et al., 2002) (Fig. 11). The doublet is particularly pronounced when the nearest cationic shell contains only Mg and/or Al atoms and is less when this shell also contains transition elements such as in Zn-Al layer double hydroxide and high Zn-containing phyllosilicate. Therefore, this spectral feature is a robust and reliable indicator of the composition, and somehow to the nature, of the Zn-bearing compound. The screening of spectra in our database showed a remarkable similarity between spectrum P-3 and lithiophorite, in which Zn fills the vacant site of the gibbsitic layer (Fig. 10b) (Manceau et al., 2000b). All other Mg- and Al-containing references gave poorer matches. This interpretation is consistent with the peak in Mn and Zn concentration measured by SXRF at this particular spot and the concomitant detection of lithiophorite by  $\mu\text{XRD}$ .

The spectral sensitivity to our Zn species identification is

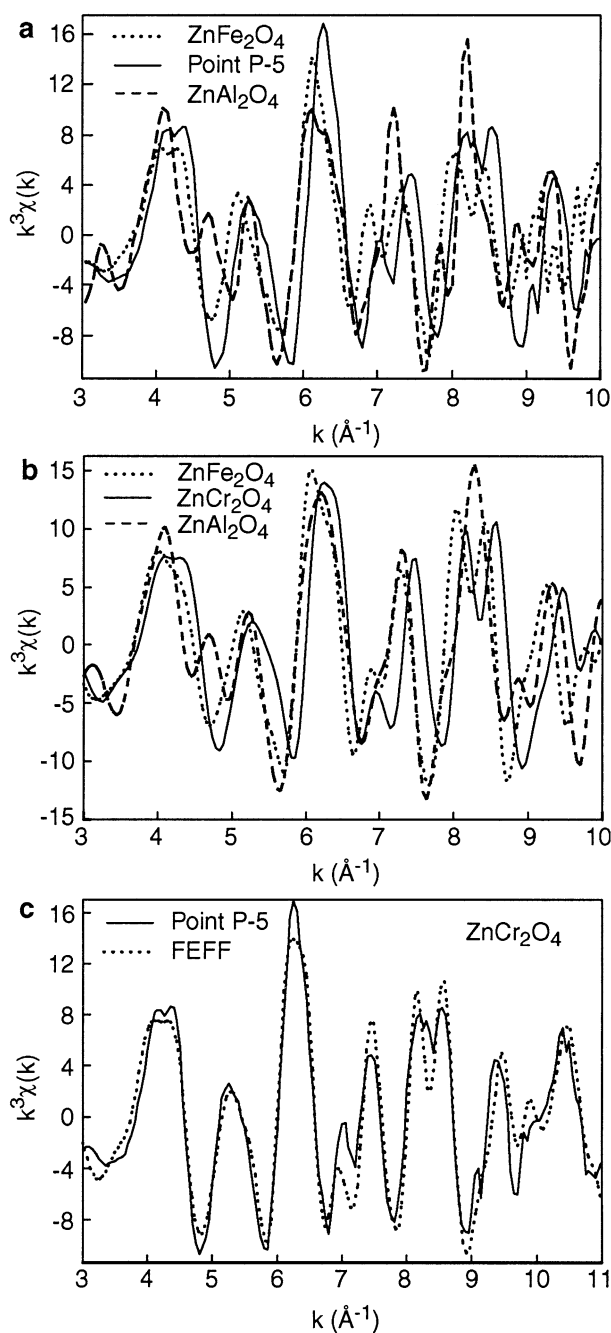


Fig. 9. (a) Experimental  $k^3$ -weighted Zn-EXAFS spectrum collected at point P-5 together with gahnite and franklinite. (b) FEFF simulations of the EXAFS spectra for gahnite, franklinite and zincochromite. (c) Experimental spectrum at point P-5 and theoretical spectrum for zincochromite calculated with the FEFF code.

illustrated in Figure 12 using the  $\mu\text{EXAFS}$  spectrum P-1 collected in the thick clay coating of the large void shown in Figure 2a. The one-component fit to spectrum P-1 identified Zn-sorbed hydroxy-Al interlayered phyllosilicate as the statistically most likely species (Fig. 12a). Assuming the presence of either lithiophorite or Zn-substituted phyllosilicate was significantly less satisfactory as shown by the doubling of the Sum-sq value and the obvious poorer matching of spectra seen

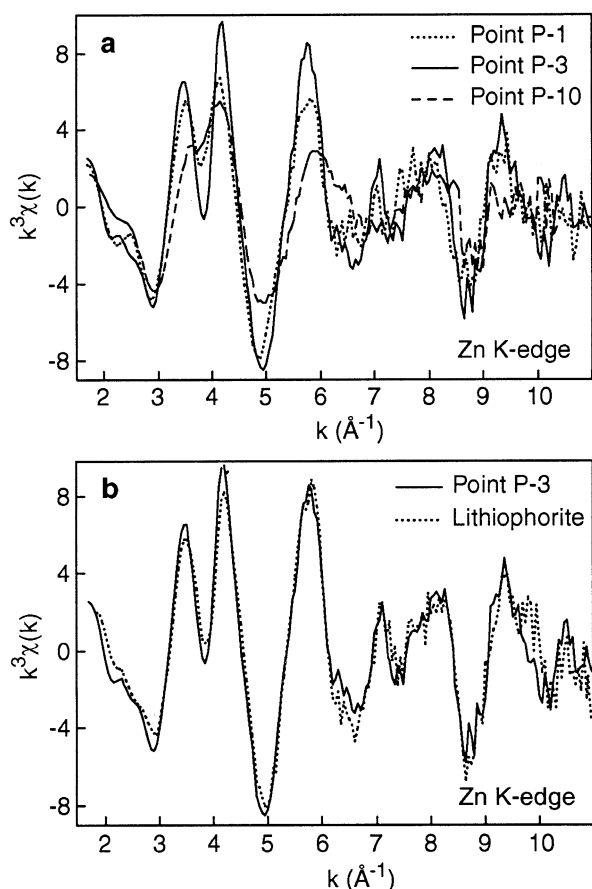


Fig. 10. (a)  $k^3$ -weighted Zn- $\mu$ EXAFS spectra collected at three points of interest (P-1, P-3 and P-10) having variable chemical compositions and, hence, variable proportions of Zn species. The three  $\mu$ EXAFS spectra are markedly different and clearly do not belong to a binary system, in which one spectrum could be reconstructed by a linear combination of the two others. (b) The spectrum recorded at point P-3 matches the Zn-containing lithiophorite reference, in which Zn substitutes for Li in the gibbsitic layer. Sum-sq value = 0.06, fraction = 94%.

in Figures 12b and 12c. The possible presence of Zn-sorbed gibbsite was discarded because, according to the data of Roberts et al. (2003), zinc forms mixed tetrahedral and octahedral complexes on the gibbsite surface, so that the presence of  $^{115}\text{Zn}$  would have modified the frequency of the EXAFS spectrum since  $d(^{115}\text{Zn-O}) < d(^{67}\text{Zn-O})$ . Although the Zn-sorbed HIM reference provides a relatively good match to the unknown spectrum, this model fails to reproduce fully the hump at  $2.5 \text{ \AA}^{-1}$  and the relative intensities of the two local maxima of the spectral doublet at  $3.5$  to  $4.1 \text{ \AA}^{-1}$ . Since this EXAFS region has a high S/N ratio, this difference is undoubtedly statistically significant. A two-component fit was attempted and combining Zn-sorbed HIM with low-Zn phyllosilicate gave the best fit with a halving of the Sum-sq value (Fig. 13a). Close examination of the simulation confirms the good agreement between the experimental and model spectrum over the entire  $k$  range explored. This structural interpretation is consistent with the detection by XRD of hydroxy-Al vermiculite in the  $<0.2\text{-}\mu\text{m}$  bulk fraction and the almost exclusive dioctahedral phyllosilicate nature of the ferriargillan as indicated by  $\mu$ XRD.

The shift to lower  $k$  values (lower frequency) of spectrum P-10 indicates the presence of tetrahedrally-coordinated zinc in the analyzed spot (Manceau et al., 2002a). A single-species fit to the data failed, and a two-component best fit yielded two statistically equivalent phase mixtures consisting of  $66 \pm 10\%$  parhohopeite ( $\text{Zn}_3[\text{PO}_4]_2 \cdot 4[\text{H}_2\text{O}]$ ) and  $33 \pm 10\%$  spectrum P-1 (Fig. 13b), and of  $65 \pm 10\%$   $^{115}\text{Zn}$ -sorbed ferrihydrite and  $33 \pm 10\%$  spectrum P-1 (Fig. 13c). The suggestive evidence of  $^{115}\text{Zn}$ -sorbed ferrihydrite should be considered cautiously because ferrihydrite generally is a “background” ferric nanophase consistently present throughout soil matrices and all attempts to find other occurrences of this Zn species within the soil sample failed. Also, the apparent absence of Zn-Mn oxide species suggested by our least-squares fitting approach appears at variance with the Zn-Mn correlation detected by  $\mu$ SXRF in this analyzed soil region. Supporting evidence for the possible

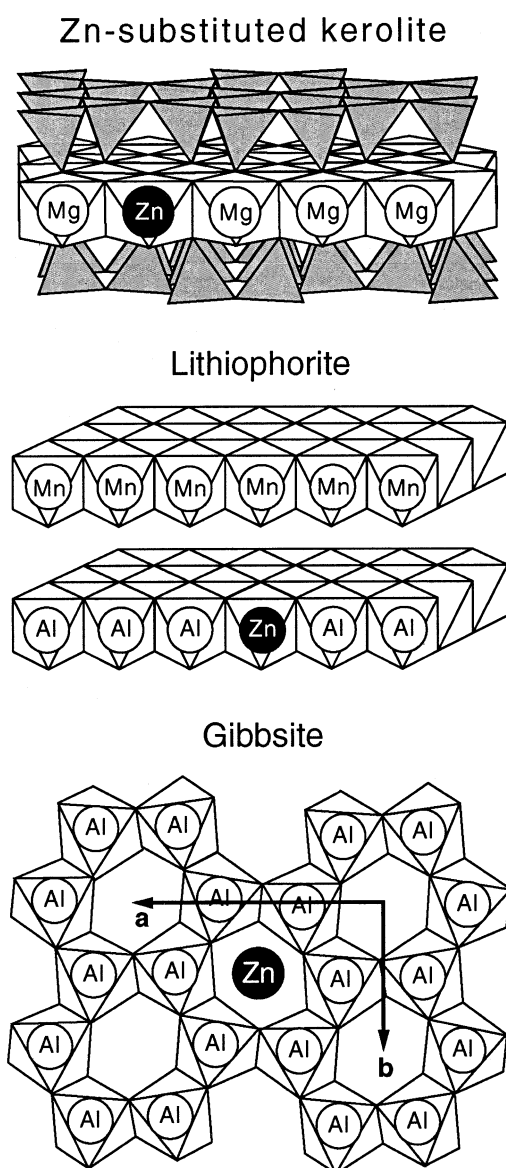


Fig. 11. Polyhedral representation of the structure of Zn-containing phyllosilicate (kerolite), lithiophorite and gibbsite.

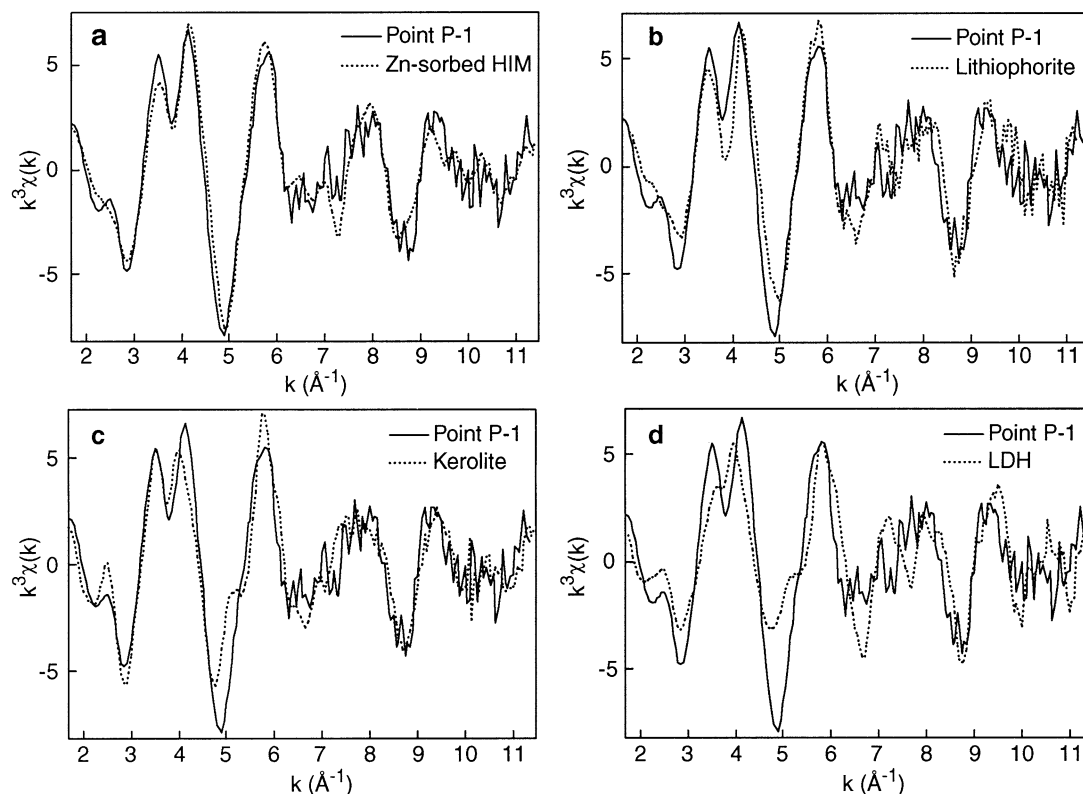


Fig. 12.  $k^3$ -weighted Zn-EXAFS spectrum collected at point P-1 compared to a selection of reference compounds: Zn-sorbed hydroxy-Al interlayered phyllosilicate, Sum-sq = 0.09, fraction = 0.96 (a), Zn-containing lithiophorite, Sum-sq = 0.17, fraction = 0.72 (b), Zn-containing kerolite ( $[Zn_{0.75}Mg_{2.25}]Si_4O_{10}[OH]_2 \cdot nH_2O$ ), Sum-sq = 0.18, fraction = 1.08 (c), and Zn-Al layered double hydroxide (LDH,  $Zn_2Al[OH]_6[CO_3]_{0.5}$ ), Sum-sq = 0.38, fraction = 0.73 (d). Kerolite is used as a proxy for the general class of Zn-containing phyllosilicate.

presence of Zn-phosphate (modeled here with parahopeite) might have been obtained by mapping the distribution of phosphorus in the sample and calculating the Zn-P correlation, but for technical reasons this was not carried out in the present study.

As many as five to six Zn species (sphalerite, zincochromite, Zn-containing phyllosilicate and lithiophorite, and possibly Zn-sorbed ferrihydrite or Zn-phosphate) were identified or inferred on a point basis, but probing with micrometer lateral resolution provides no idea of the representativity of each species in the bulk sample. The fractional amount of each Zn species was determined from an EXAFS spectrum of powdered soil obtained using a beam size of 300  $\mu\text{m}$  FWHM. The FAME X-ray absorption spectrometer (ESRF) was used because it yields an integrated flux about two orders of magnitude higher than can be obtained at 10.3.2 (ALS) ( $\sim 10^{12}$  vs.  $10^{10}$  photons). Nonetheless, Figure 14 shows that the bulk and point spectra have similar S/N ratio, illustrating the difficulty of studying the average form of trace elements by bulk EXAFS in heterogeneous natural matrices. In the present sample, the concentration of Zn averages 128 mg/kg, but may be as high as several thousands of milligrams per kilogram in hot spots. The heterogeneity of the Zn distribution effectively dilutes the fraction of photons interacting with the metal in a bulk EXAFS measurement, and thus, a higher total incident flux is required to obtain the same signal as in a point analysis. Another difficulty is

caused by the abundance of iron, whose strong  $K\alpha$  radiation obscures the fluorescence signal of zinc. Here, the background-to-signal ratio was  $>700:1$  considering the high Fe/Zn ratio ( $\sim 720$ ) and the parasitic coherent (elastic) and incoherent (Compton) scattering signal from the incoming beam. Finally, the greater number of structural environments for Zn above the micrometer scale yields a lower amplitude signal and, hence, a lower S/N ratio for a given experimental setup. The similar bulk EXAFS and  $\mu$ -EXAFS spectra of Zn shown in Figure 14 demonstrate that the Zn species identified at points P-3, P-5, P-6, P-10 are present in minor amounts ( $<5$ – $10\%$  of total Zn) in the bulk sample. Therefore, Zn is associated primarily with phyllosilicates in the bulk analysis, but its form is not unique. Reconstruction of the micrometer-scale P-1 spectrum suggested two Zn binding sites: Zn substituting in octahedral sheets, and Zn sorbed to hydroxy-Al entities possibly located within the interlayer region of vermiculite identified by XRD.

## 4. DISCUSSION

### 4.1. Sequestration Mechanism of Zn and Ni in Lithiophorite

In the studied sample, lithiophorite is a minor species because of the essentially clayey nature of the soil and the paucity of manganese. However, previous (Manceau et al., 2003) and

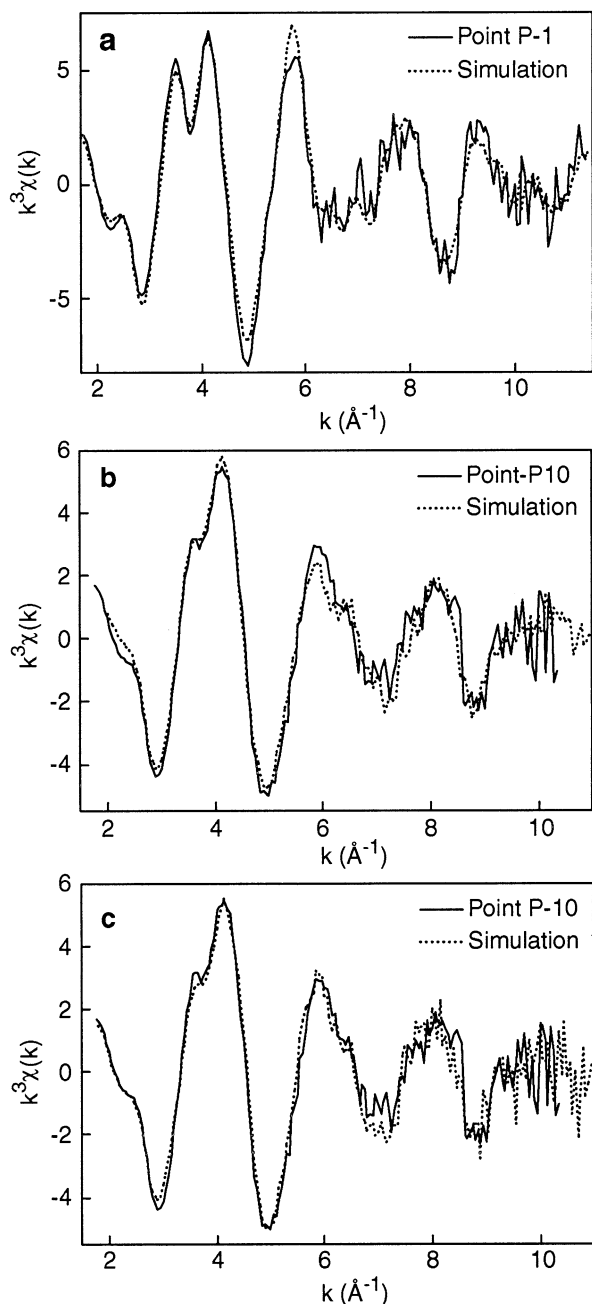


Fig. 13. Two-component fits of spectra collected at points P-1 (a) and P-10 (b, c). P-1 was best simulated (Sum-sq = 0.05) assuming a mixture of Zn-sorbed hydroxy-Al interlayered phyllosilicate and Zn-containing phyllosilicate, in proportions of 66 and 42%, respectively (estimated accuracy 10% of the total zinc). The spectrum P-10 could be reproduced satisfactorily by two statistically equivalent combinations: one consisting of a mixture of spectra P-1 and Zn-phosphate (Sum-sq = 0.06) (b), and another consisting of a mixture of spectra P-1 and Zn-sorbed ferrihydrite (Sum-sq = 0.07) (c).

on-going studies provide evidence that Zn-lithiophorite (ZnLi) may prevail over phyllosilicate in manganiferous matrices, and lithiophorite was shown to be one of the main scavengers of nickel in soils (Manceau et al., 2002c). The high affinity of nickel for soil lithiophorite was explained by the abundance of

trivalent manganese within the manganese layer and the similar, but slightly larger, size of  $\text{Ni}^{2+}$  ( $r = 0.69 \text{ \AA}$ ) relative to  $\text{Mn}^{3+}$  ( $r = 0.645 \text{ \AA}$ ), since impurities are energetically better stabilized in smaller crystallographic sites (Davies et al., 2000). As will be shown below, charge balance and steric effects also likely account for the specific incorporation of zinc within the gibbsitic layer of lithiophorite (Fig. 11). In a similar manner to all dioctahedral layer frameworks, two of the three octahedral positions per half unit cell are occupied in gibbsite ( $\alpha\text{-Al}(\text{OH})_3$ ), with the filled sites being much smaller ( $\langle d(\text{Al}-\text{O}) \rangle = 1.90 \text{ \AA}$ ) than the empty sites ( $\langle d(\square-\text{O}) \rangle = 2.13 \text{ \AA}$ ) (Saalfeld and Wedde, 1974). The precise structure of the gibbsitic layer of lithiophorite is unknown but thought to be similar to that of gibbsite, differing only by the partial filling of empty sites by foreign cations (ideally by  $\text{Li}^+$ ) to compensate the negative charge of the manganese layer resulting from the  $\text{Mn}^{3+}$  for  $\text{Mn}^{4+}$  substitutions (Post and Appleman, 1994). At least three factors contribute to specifically sequester Zn in the gibbsitic layer of lithiophorite: (1) the similarity in size of lithium and zinc since they differ by only two hundredths of an angstrom (0.76 vs. 0.74  $\text{\AA}$ , respectively); (2) the general higher sorption affinity of divalent over monovalent cations for mineral surfaces; and (3) the size of the empty octahedral cage which, with a metal center-oxygen distance of 2.13  $\text{\AA}$ , precisely matches the average value for Zn in octahedral coordination with oxygen (2.11  $\text{\AA}$ , Sarret et al., 1998; Waychunas et al., 2002). Although zinc and nickel are sequestered by two different structural mechanisms in soil lithiophorite, they both contribute to enhance the stability of the  $\text{Al}(\text{OH})_3\text{-MnO}_2$  mixed-layer structure in a contrasted, but complementary, manner: zinc in yielding a positive charge to the aluminous layer, and nickel in providing a negative charge to the manganiferous layer. This example illustrates the role of point defects in the stabilization of mineral structures. Therefore, lithiophorite can be viewed as an accomplished scavenger of trace metals in soils since they enhance the stability, and hence favor the formation, of this layered double oxyhydroxide (LDO) phase.

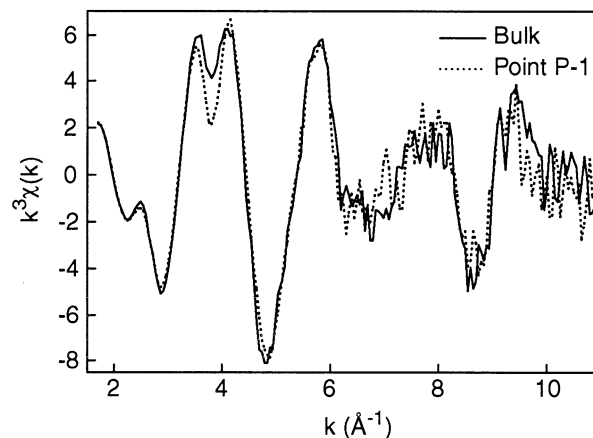


Fig. 14. Comparison of the Zn- $\mu$ EXAFS spectrum collected at point P-1 and the bulk Zn-EXAFS spectrum obtained from a powder of the soil material. The overall likeness of these two EXAFS spectra (compare the shape of these two EXAFS spectra with those presented in Figs. 7 and 10a) indicates that Zn is predominantly associated with the phyllosilicate fraction, and that the other species identified by  $\mu$ EXAFS are present in subordinate amounts in the soil.

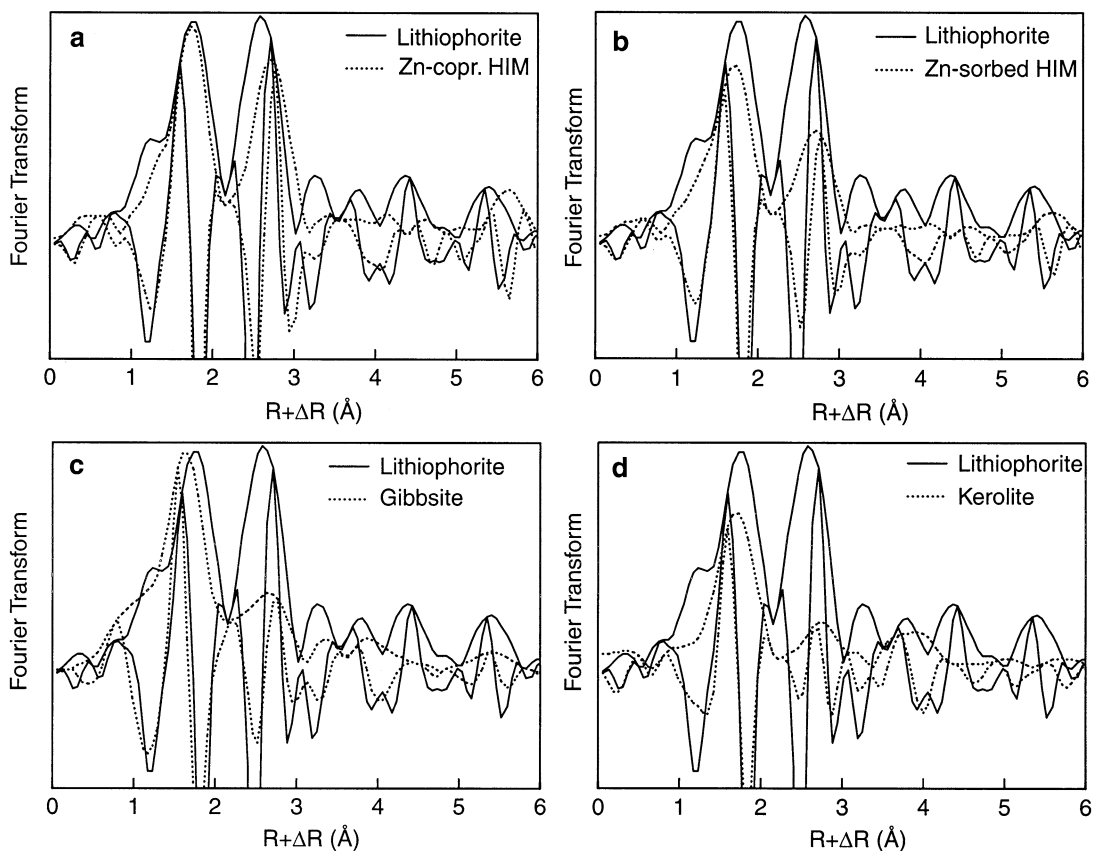


Fig. 15. Comparison of the Fourier transform (FT) for Zn-containing soil lithiophorite to FTs of four references: Zn-coprecipitated and Zn-sorbed hydroxy-Al interlayered phyllosilicate (a, b), Zn-sorbed gibbsite (c), and Zn-containing phyllosilicate (kerolite,  $[\text{Zn}_{0.75}\text{Mg}_{2.25}]\text{Si}_4\text{O}_{10}[\text{OH}]_2 \cdot n\text{H}_2\text{O}$ ) (d). For the sake of clarity, the FT for Zn-sorbed gibbsite was multiplied by 1.75.

#### 4.2. Local Structure of Zn in the Gibbsitic Layer of Lithiophorite

As we view the various forms of Zn identified or inferred in the present study, and in particular the exquisite role of lithiophorite and phyllosilicate in the scavenging of zinc in soils, one question comes to mind: Is it possible to distinguish by EXAFS spectroscopy ZnLi from low Zn-containing (Al,Mg)-phyllosilicate, Zn-sorbed gibbsite, and Zn-sorbed and Zn-coprecipitated hydroxy-Al interlayer species? In all these compounds, Zn atoms are neighbored by Al and/or Mg atoms from a gibbsitic (Al) or brucitic (Mg) edge-sharing framework at  $\sim 3.0$  Å (first-cationic shell),  $3.0 \times \sqrt{3} = 5.20$  Å (second-cationic shell), and  $3.0 \times 2 = 6.0$  Å (third-cationic shell). A direct consequence from this particular local structure is the split of the first EXAFS oscillation at  $k \sim 3.8$  Å<sup>-1</sup> (Manceau et al., 1987, 2000b), which is now being used as a powerful spectroscopic fingerprint for this type of structural environment in unknown materials (Roberts et al., 2002, 2003; Scheinost et al., 2002). Note that Zn-Al layered double hydroxide (Zn-Al LDH) and high Zn phyllosilicates are excluded from this group of compounds because in LDH Zn is neighbored both by “light” (i.e., Al) and “heavy” (i.e., Zn) atoms, resulting in the disappearance of the double beat (Fig. 12 and Schlegel et al., 2001). Figure 15 shows that lithiophorite has a distinctly different Fourier trans-

form from Zn-sorbed gibbsite and Zn-sorbed/copr. HIM: the last two have a longer Zn-Al bond distance as attested by the shift to higher  $R + \Delta R$  values of both the magnitude and imaginary part of the Fourier transforms. In addition, Zn has a significantly smaller Zn-O bond distance in Zn-sorbed gibbsite according to Roberts et al. (2003). The observed differences can be rationalized in terms of Zn coordination, i.e., nature and strain of the Zn site. In Zn-sorbed gibbsite, Roberts et al. (2003) reported a Zn-O bond distance (2.00–2.02 Å) intermediate between those for octahedral ( $\sim 2.10$  Å) and tetrahedral ( $\sim 1.95$  Å) coordination (Sarret et al., 1998; Waychunas et al., 2002), which they attributed to the formation of a mixed Zn coordination complex at the gibbsite surface. In lithiophorite, Zn substitutes for Li in the gibbsitic layer and its pure octahedral coordination, together with the presence of six nearest Al neighbors which on the Fourier transform gives rise to an intense metal shell peak at  $\sim R + \Delta R = 2.6$  Å, afford a way to distinguish Zn in lithiophorite from sorption complexes on Al hydroxide compounds. However, the shortening of the Zn-Al distance in the aluminous layer of lithiophorite ( $d[\text{Zn-Al}] \sim 3.00$  Å) provides the best criterion to the differentiation of ZnLi from gibbsite and other pure aluminum hydroxides. Low Zn-containing phyllosilicate has its second peak’s imaginary part in phase with ZnLi, but the metal shell FT magnitude is

different. Figure 15d shows that the imaginary part reaches a maximum to the left side of the FT magnitude, whereas it peaks to the right side in pure aluminous compounds. The shift in the relative positions of the two FT functions in the  $[2.3\text{--}3.0 \text{ \AA}] R + \Delta R$  interval indicates that Zn has a different cationic environment in the two kinds of materials. Quantitative analysis of the low Zn-containing phyllosilicate (Schlegel et al., 2001) revealed that the second peak results from the interfering contribution from nearest cations in the octahedral (here Mg atoms at  $\sim 3.07 \text{ \AA}$ ) and tetrahedral (Si atoms at  $\sim 3.24 \text{ \AA}$ ) sheets. The destructive interference of the Zn-Mg and Zn-Si waves over most of the  $k$  space accounts for the reduction in amplitude of the second RSF peak relative to ZnLi. The phyllosilicate RSF also has a lower first peak owing to the wider range of bond lengths caused by the coordination of Zn atoms to both oxygen and hydroxyl ligands in hydrous silicates. The same holds true for Zn-sorbed Al hydroxide compounds in which surface Zn atoms are coordinated at least to hydroxyls and water molecules, and possibly also to oxygens. Consistent with these observations, the first RSF peaks for ZnLi and Zn-copr., in which Zn is coordinated to only one type of ligand (OH), have the same amplitude.

**Acknowledgments**—The soil sample was provided by J. M. Bigham, and the EXAFS spectra for Zn-sorbed and Zn-coprecipitated hydroxy-Al interlayered phyllosilicate, and for Zn-sorbed gibbsite, were provided by A. C. Scheinost and D. R. Roberts, respectively. The authors acknowledge scientific advice from three anonymous reviewers. The ALS and the ESRF are thanked for the provision of beamtime, and J. L. Hazemann for his assistance during EXAFS measurements on FAME (ESRF). This work was partly supported by the Director, Office of Energy Research, Office of Basic Energy Sciences, Materials Sciences Division of the U.S. Department of Energy, under Contract No. DE-AC03-76SF00098.

*Associate editor:* D. J. Vaughan

## REFERENCES

- Adriano D. C. (1986) Trace Elements in the Terrestrial Environment. Springer-Verlag, New York.
- Brewer R. (1976) Fabric and Mineral Analysis of Soils. Robert E. Krieger, Malabar, FL.
- Carroll S., O'Day P. A., Esser B., and Randall S. (2002) Speciation and fate of trace metals in estuarine sediments under reduced and oxidized conditions, Seaplane Lagoon, Alameda Naval Air Station (USA). *Geochem. Trans.* **3**, 81–101.
- Chaney R. L. (1993) Zinc phytotoxicity. In *Zinc in Soils and Plants* (ed. A. D. Robson), pp. 135–155. Kluwer Academic, Dordrecht, the Netherlands.
- Chen Z. S., Tsou T. C., Asio V. B., and Tsai C. C. (2001) Genesis of ineptisols on a volcanic landscape in Taiwan. *Soil Sci.* **166**, 255–266.
- Davies R. A., Islam M. S., Chadwick A. V., and Rush G. E. (2000) Cation dopant sites in the  $\text{CaZrO}_3$  proton conductor: A combined EXAFS and computer simulation study. *Solid State Ionics* **130**, 115–122.
- Douglas L. A. (1989) Vermiculites. In *Minerals in Soil Environments* (eds. J. B. Dixon and S. B. Weed), pp. 635–728. Soil Science Society of America, Madison, WI.
- Drits V. A., Silvester E., Gorshkov A. I., and Manceau A. (1997) The structure of synthetic monoclinic Na-rich birnessite and hexagonal birnessite. Part I. Results from X-ray diffraction and selected area electron diffraction. *Am. Mineral.* **82**, 946–961.
- FitzPatrick E. A. (1993) Soil Microscopy and Micromorphology. John Wiley, New York.
- Gaillard J. F., Webb S. M., and Quintana J. P. G. (2001) Quick X-ray absorption spectroscopy for determining metal speciation in environmental samples. *J. Synch. Rad.* **8**, 928–930.
- Hansel C. M., Fendorf S., Sutton S., and Newville M. (2001) Characterization of Fe plaque and associated metals on the roots of mine-waste impacted aquatic plants. *Environ. Sci. Technol.* **35**, 3863–3868.
- Hseu Z. Y. and Chen Z. S. (1997) Soil hydrology and micromorphology of illuvial clay in an Ultisol hydrosequence. *J. Chin. Agri. Chem. Soc.* **35**, 503–512.
- Hseu Z. Y. and Chen Z. S. (1999) Micromorphology of redoximorphic features of subtropical anthraquic Ultisols. *Food Sci. Agri. Chem.* **1**, 194–202.
- Isaure M. P., Laboudigue A., Manceau A., Sarret G., Tiffreau C., Trocellier P., Hazemann J. L., and Chateigner D. (2002) Quantitative Zn speciation in a contaminated dredged sediment by  $\mu\text{PIXE}$ ,  $\mu\text{SXRF}$ , EXAFS spectroscopy and principal component analysis. *Geochim. Cosmochim. Acta* **66**, 1549–1567.
- Isaure M. P., Manceau A., Laboudigue A., Tamura N. and Marcus M. A. (2003) Zn speciation in a soil contaminated by the deposition of a dredged sediment by synchrotron X-ray techniques. *Journal de Physique* **107**, 657–660.
- Juillot F., Morin G., Ildefonse P., Trainor T. P., Benedetti M., Galois L., Calas G., and Brown G. E., Jr. (2003) Occurrence of Zn/Al hydroxalite in smelter-impacted soils from northern France: Evidence from EXAFS spectroscopy and chemical extractions. *Am. Mineral.* **88**, 509–526.
- Kirpichtchikova T., Manceau A., Lanson B., Sarret G., Marcus M. A. and Jacquet T. (2003) Speciation and mobility of heavy metals (Zn, Cu and Pb) in soil contaminated by sewage irrigation. *Journal de Physique* **107**, 695–698.
- Lanson B., Drits V. A., Silvester E. J., and Manceau A. (2000) Structure of H-exchanged hexagonal birnessite and its mechanism of formation from Na-rich monoclinic buserite at low pH: New data from X-ray diffraction. *Am. Mineral.* **85**, 826–835.
- Lanson B., Drits V. A., Feng Q., and Manceau A. (2002) Crystal structure determination of synthetic Na-rich birnessite: Evidence for a triclinic one-layer cell. *Am. Mineral.* **87**, 1662–1671.
- Luther G. W., III, Meyerson A. L., Krajewski J., and Hires R. I. (1980) Metal sulfides in estuarine sediments. *J. Sedim. Petr.* **50**, 1117–1120.
- Luther G. W., III, Rickard D., Theberge S. M., and Olroyd A. (1996) Determination of metal (bisulfide) stability constants of Mn, Fe, Co, Ni, Cu and Zn by voltammetric methods. *Environ. Sci. Technol.* **30**, 671–679.
- Malla P. B. and Douglas L. A. (1987) Identification of expanding layer silicates: Charge density vs. expansion properties. In *8th International Clay Conference* (eds. L. G. Schultz, H. van Olphen, and F. A. Mumpton), pp. 277–283. Clay Minerals Society, Bloomington, IN.
- Manceau A., Llorca S., and Calas G. (1987) Crystal chemistry of cobalt and nickel in lithiophorite and asbolane from New Caledonia. *Geochim. Cosmochim. Acta* **51**, 105–113.
- Manceau A., Boisset M. C., Sarret G., Hazemann J. L., Mench M., Cambier P., and Prost R. (1996) Direct determination of lead speciation in contaminated soils by EXAFS spectroscopy. *Environ. Sci. Technol.* **30**, 1540–1552.
- Manceau A., Drits V. A., Silvester E., Bartoli C., and Lanson B. (1997) Structural mechanism of Co(II) oxidation by the phyllo-manganate, Na-buserite. *Am. Mineral.* **82**, 1150–1175.
- Manceau A., Chateigner D., and Gates W. P. (1998) Polarized EXAFS, distance-valence least-squares modeling (DVLS) and quantitative texture analysis approaches to the structural refinement of Garfield nontronite. *Phys. Chem. Miner.* **25**, 347–365.
- Manceau A., Lanson B., Schlegel M. L., Hargé J. C., Musso M., Eybert-Bérard L., Hazemann J. L., Chateigner D., and Lamble G. M. (2000a) Quantitative Zn speciation in smelter-contaminated soils by EXAFS spectroscopy. *Am. J. Sci.* **300**, 289–343.
- Manceau A., Schlegel M. L., Musso M., Sole V. A., Gauthier C., Petit P. E., and Trolard F. (2000b) Crystal chemistry of trace elements in natural and synthetic goethite. *Geochim. Cosmochim. Acta* **64**, 3643–3661.
- Manceau A., Lanson B., and Drits V. A. (2002a) Structure of heavy metal sorbed birnessite. Part III. Results from powder and polarized

- extended X-ray absorption fine structure spectroscopy. *Geochim. Cosmochim. Acta* **66**, 2639–2663.
- Manceau A., Marcus M. A., and Tamura N. (2002b) Quantitative speciation of heavy metals in soils and sediments by synchrotron X-ray techniques. *Rev. Mineral. Geochem.* **49**, 341–428.
- Manceau A., Tamura N., Marcus M. A., MacDowell A. A., Celestre R. S., Sublett R. E., Sposito G., and Padmore H. A. (2002c) Deciphering Ni sequestration in soil ferromanganese nodules by combining X-ray fluorescence, absorption and diffraction at micrometer scales of resolution. *Am. Mineral.* **87**, 1494–1499.
- Manceau A., Tamura N., Celestre R. S., MacDowell A. A., Geoffroy N., Sposito G., and Padmore H. A. (2003) Molecular-scale speciation of Zn and Ni in soil ferromanganese nodules from loess soils of the Mississippi basin. *Environ. Sci. Technol.* **37**, 75–80.
- Marques J. J., Teixeira W. G., Schulze D. G., and Curi N. (2002) Mineralogy of soils with unusually high exchangeable Al from the western Amazon Region. *Clay Miner.* **37**, 651–661.
- Moore D. M. and Reynolds R. C. J. (1997) X-Ray Diffraction and the Identification and Analysis of Clay Minerals. Oxford University Press, New York.
- Mustre de Leon J., Rehr J. J., Zabinsky S. I., and Albers R. C. (1991) Ab initio curved-wave X-ray-absorption fine structure. *Phys. Rev. B* **44**, 4146–4156.
- Nesterov A. R. and Rumyantseva Y. V. (1987) Zincochromite  $ZnCr_2O_4$ —A new mineral from Karelia [in Russian]. *Zapiski Vses. Mineralog. Obshch.* **116**, 367–371.
- O'Day P. A., Rehr J. J., Zabinsky S. I., and Brown G. E., Jr (1994) Extended X-ray absorption fine structure (EXAFS) analysis of disorder and multiple-scattering in complex crystalline solids. *J. Am. Chem. Soc.* **116**, 2938–2949.
- O'Day P. A., Carroll S. A., and Waychunas G. A. (1998) Rock-water interactions controlling zinc, cadmium, and lead concentrations in surface waters and sediments, U.S. Tri-State Mining District. I. Molecular identification using X-ray absorption spectroscopy. *Environ. Sci. Technol.* **32**, 943–955.
- O'Day P. A., Carroll S. A., Randall S., Martinelli R. E., Anderson S. L., Jelinski J., and Knezovich J. P. (2000) Metal speciation and bio-availability in contaminated estuary sediments, Alameda Naval Air Station, California. *Environ. Sci. Technol.* **34**, 3665–3673.
- O'Neill H. S. C. and Dollase W. A. (1994) Crystal structures and cation distributions in simple spinels from powder XRD structural refinements:  $MgCr_2O_4$ ,  $ZnCr_2O_4$ ,  $Fe_3O_4$  and the temperature dependence of the cation distribution in  $ZnAl_2O_4$ . *Phys. Chem. Miner.* **20**, 541–555.
- Ostergren J. D., Brown G. E., Parks G. A., and Tingle T. N. (1999) Quantitative lead speciation in selected mine tailings from Leadville, CO. *Environ. Sci. Technol.* **33**, 1627–1636.
- Parkman R. H., Curtis C. D., Vaughan D. J., and Charnock J. M. (1996) Metal fixation and mobilisation in the sediments of Afon Goch estuary—Dulas Bay, Anglesey. *Appl. Geochem.* **11**, 203–210.
- Post J. E. and Appleman D. E. (1994) Crystal structure refinement of lithiophorite. *Am. Mineral.* **79**, 370–374.
- Ressler T., Wong J., Roos J., and Smith I. (2000) Quantitative speciation of Mn-bearing particulates emitted from autos burning methylcyclopentadienyl manganese tricarbonyl- (MMT-) added gasolines using XANES spectroscopy. *Environ. Sci. Technol.* **34**, 950–958.
- Roberts D. R., Scheinost A. C., and Sparks D. L. (2002) Zinc speciation in a smelter-contaminated soil profile using bulk and microscopic techniques. *Environ. Sci. Technol.* **36**, 1742–1750.
- Roberts D. R., Ford R. G., and Sparks D. L. (2003) Kinetics and mechanisms of Zn complexation on metal oxides using EXAFS spectroscopy. *J. Colloid Interface Sci.* **263**, 364–376.
- Robson A. D. (1993) Zinc in Soils and Plants. Kluwer Academic, Dordrecht, the Netherlands.
- Ross D. S., Hales H. C., Sea-McCarthy G. C., and Lanzirrotti A. (2001) Sensitivity of soil manganese oxides: XANES spectroscopy may cause reduction. *Soil Sci. Soc. Am. J.* **65**, 744–752.
- Saalfeld H. and Weddeý M. (1974) Refinement of the crystal structure of gibbsite,  $Al(OH)_3$ . *Zeit. Kristall.* **139**, 129–135.
- Sarret G., Manceau A., Cuny D., Van Haluwyn C., Déruelle S., Hazemann J. L., Eybert-Bérard L., and Menthonnex J. J. (1998) Molecular mechanisms of Pb and Zn hyperaccumulation and tolerance in lichens. *Environ. Sci. Technol.* **32**, 3325–3330.
- Sawada H. (1997) Electron density study of spinels: Zinc chromium oxide. *Mater. Res. Bull.* **32**, 873–879.
- Scheinost A. C., Kretzschmar R., Pfister S., and Roberts D. R. (2002) Combining selective sequential extractions, X-ray absorption spectroscopy and principal component analysis for quantitative zinc speciation in soil. *Environ. Sci. Technol.* **36**, 5021–5028.
- Schlegel M. L., Manceau A., Charlet L., and Hazemann J. L. (2001) Adsorption mechanism of Zn on hectorite as a function of time, pH, and ionic strength. *Am. J. Sci.* **301**, 798–830.
- Schwertmann U. and Taylor R. M. (1989) Iron Oxides. Soil Science Society of America, Madison, WI.
- Sepelak V., Tkacova K., Boldyrev V. V., and Steinike U. (1996) Crystal structure refinement of the mechanically activated spinelferrite. *Mater. Sci. Forum* **228**, 783–788.
- Silvester E., Manceau A., and Drits V. A. (1997) The structure of synthetic monoclinic Na-rich birnessite and hexagonal birnessite. Part 2. Results from chemical studies and EXAFS spectroscopy. *Am. Mineral.* **82**, 962–978.
- Singh B. and Gilkes R. J. (1996) Nature and properties of iron rich glauabules and mottles from some south-west Australian soils. *Geoderma* **71**, 95–120.
- Smek N. E., Bigham J. M., Guertel W. F., and Hall G. F. (2002) Spatial distribution of lepidocrocite in a soil hydrosequence. *Clay Miner.* **37**, 687–697.
- Strawn D., Doner H., Zavarin M., and McHugo S. (2002) Microscale investigation into the geochemistry of arsenic, selenium and iron in soil developed in pyritic shale materials. *Geoderma* **108**, 237–257.
- Tebo B. M., Ghiorse W. C., van Waasbergen L. G., Siering P. L., and Caspi R. (1997) Bacterially mediated mineral formation: Insights into manganese(II) oxidation from molecular genetic and biochemical studies. *Rev. Mineral.* **35**, 225–266.
- Vetter K. J. and Jaeger N. (1966) Potentialausbildung an der Mangan-dioxid-elektrode als Oxidelektrode mit nichtstöchiometrischem Oxid. *Electrochim. Acta* **11**, 401–419.
- Villalobos M., Toner B., Bargar J., and Sposito G. (2003) Characterization of the manganese oxide produced by *Pseudomonas putida* strain MnB1. *Geochim. Cosmochim. Acta* **67**, 2649–2662.
- Waychunas G. A., Fuller C. C., and Davis J. A. (2002) Surface complexation and precipitate geometry for aqueous Zn(II) sorption on ferrihydrite I: X-ray absorption extended fine structure spectroscopy analysis. *Geochim. Cosmochim. Acta* **66**, 1119–1137.
- Yang D. S. and Wang M. K. (2003) Characterization and a fast method for synthesis of sub-micron lithiophorite. *Clays Clay Miner.* **51**, 96–101.